

Non-degenerate, three-wave mixing with the Josephson ring modulator

Baleegh Abdo,* Archana Kamal, and Michel Devoret
Department of Applied Physics, Yale University, New Haven, CT 06520, USA.

(Dated: August 20, 2018)

The Josephson ring modulator (JRM) is a device, based on Josephson tunnel junctions, capable of performing non-degenerate mixing in the microwave regime without losses. The generic scattering matrix of the device is calculated by solving coupled quantum Langevin equations. Its form shows that the device can achieve quantum-limited noise performance both as an amplifier and a mixer. Fundamental limitations on simultaneous optimization of performance metrics like gain, bandwidth and dynamic range (including the effect of pump depletion) are discussed. We also present three possible integrations of the JRM as the active medium in a different electromagnetic environment. The resulting circuits, named Josephson parametric converters (JPC), are discussed in detail, and experimental data on their dynamic range are found to be in good agreement with theoretical predictions. We also discuss future prospects and requisite optimization of JPC as a preamplifier for qubit readout applications.

PACS numbers: 84.30.Le, 85.25.Cp, 85.25.-j, 42.60.Da

The photon energy of microwave radiation in the band from 4 – 8 GHz ($\sim 8 - 4$ cm wavelength) is approximately 10^5 smaller than that of the visible light. Yet, at a temperature 10^4 smaller than room temperature, now routinely achievable with a dilution refrigerator, it is now possible to resolve the energy of single microwave photons¹. There are three advantages of single photon microwave electronics when compared with quantum optics. First, signal shapes at carrier frequencies of a few GHz with a relative bandwidth of few percent can be controlled with much greater relative precision than their equivalent at a few hundreds of THz. This is partly due to the fact that microwave generators have more short term stability than lasers, but also because microwave components are mechanically very stable, particularly when cooled, compared with traditional optical components. Second, in single photon microwave electronics, the on-chip circuitry can be well in the lumped element regime, and spatial mode structure can be controlled more thoroughly and more reliably than in the optical domain. Finally, there exists a simple, robust non-dissipative component, the Josephson tunnel junction (JJ), whose non-linearity can be ultra-strong even at the single photon level². Many quantum signal processing functions have been realized using JJs, both digital and analog, and this short review will not attempt to describe all of them. We will focus on analog Josephson devices pumped with a microwave tone. They recently led to microwave amplifiers working at the single photon level^{3,4}. These novel devices have taken the work pioneered by B. Yurke at Bell labs 25 years ago⁵⁻⁷ to the point where actual experiments can be performed using Josephson amplifiers as the first link in the chain of measurement⁸⁻¹⁰.

In this paper, we address one particular subclass of analog signal processing devices based on Josephson tunnel junction, namely those performing non-degenerate three-wave mixing. Examples are Josephson circuits based on the Josephson ring modulator^{11,12} which we will describe below. The Hamiltonian of such a device is

of the form

$$H_0 = \frac{1}{2} \left(\frac{P_X^2}{\mathcal{M}_X} + \frac{P_Y^2}{\mathcal{M}_Y} + \frac{P_Z^2}{\mathcal{M}_Z} \right) + \frac{1}{2} (\mathcal{K}_X X^2 + \mathcal{K}_Y Y^2 + \mathcal{K}_Z Z^2) + KXYZ, \quad (1)$$

where (X, Y, Z) and (P_X, P_Y, P_Z) are the generalized position and momentum variables for the three independent oscillators, $\mathcal{M}_{X,Y,Z}$ and $\mathcal{K}_{X,Y,Z}$ represent the “mass” and “spring constant” of the relevant oscillator (see table I), and K is the three-wave mixing constant which governs the non-linearity of the system. We will discuss later how such simple minimal non-linear term can arise. The classical equation of motions for the standing waves in such a device are symmetric and are given by:

$$\ddot{X} + \gamma_a \dot{X} + \omega_a^2 X + K'YZ = x(t) \cos \omega_a t, \quad (2)$$

$$\ddot{Y} + \gamma_b \dot{Y} + \omega_b^2 Y + K'XZ = y(t) \cos \omega_b t, \quad (3)$$

$$\ddot{Z} + \gamma_c \dot{Z} + \omega_c^2 Z + K'XY = z(t) \cos \omega_c t, \quad (4)$$

where $K' = K/\mathcal{M}$ (we assume, for simplicity, equal masses $\mathcal{M}_{X,Y,Z} = \mathcal{M}$) and $\omega_{a,b,c} = \sqrt{\mathcal{K}_{X,Y,Z}/\mathcal{M}}$ are the angular resonant frequencies of the three coordinates satisfying

$$\omega_a < \omega_b < \omega_c = \omega_a + \omega_b. \quad (5)$$

We also suppose the oscillators are well in the underdamped regime

$$\gamma_a \ll \omega_a, \quad (6)$$

$$\gamma_b \ll \omega_b, \quad (7)$$

$$\gamma_c \ll \omega_c, \quad (8)$$

a sufficient but not strictly necessary hypothesis, which has the principal merit of keeping the problem analytically soluble under the conditions of interest. It is worth

X (position)	P (momentum)	\mathcal{M} (mass)	\mathcal{K} (spring constant)
Φ (flux)	Q	C (capacitance)	L^{-1}
Q (charge)	Φ	L (inductance)	C^{-1}

TABLE I: Generalized variables and parameters for the system of oscillators described by Eq. (1). The variables and parameters listed in the first line apply to the case of a mechanical oscillator, whereas the ones listed in the second and third lines are adapted for describing an LC oscillator with parallel and series dissipations, respectively, as shown in Fig. 1 and Fig. 16 (top panel) for the parallel case, and Fig. 16 (bottom panel) for the series case.

noting that the system is non-degenerate both spatially and temporally. On the other hand, it is important to suppose that the envelope functions $x(t)$, $y(t)$ and $z(t)$ of the drive signals are supposed to be slow compared to the respective drive frequencies $\omega_b - \omega_a \gg \gamma_a + \gamma_b$.

The equations (2-4) must be contrasted with that of a degenerate three-wave mixing device for which two cases are possible. In the first case, where the Y and Z degrees of freedom have merged into a single oscillator, the Hamiltonian has a non-linear term of the form KXZ^2 and the equations read:

$$\ddot{X} + \gamma_a \dot{X} + \omega_a^2 X + K'Z^2 = x(t) \cos \omega_a t, \quad (9)$$

$$\ddot{Z} + \gamma_c \dot{Z} + \omega_c^2 Z + 2K'ZX = z(t) \cos \omega_c t. \quad (10)$$

This is the case of electromechanical resonators¹³ in which one of the capacitance plates of a microwave oscillator (Z) is itself the mass of a mechanical resonator (X). There $\omega_c \gg \omega_a$, and pumping the microwave oscillator in the vicinity of $\omega_c - \omega_a$ leads to cooling of the mechanical oscillator provided $\gamma_c \gg \gamma_a$. In the second case, it is the X and the Y degrees of freedom that merge into a single oscillator, leading to a non-linear term in the Hamiltonian of the form KX^2Z . The equations then read

$$\ddot{X} + \gamma_a \dot{X} + \omega_a^2 X + 2K'XZ = x(t) \cos \omega_a t, \quad (11)$$

$$\ddot{Z} + \gamma_c \dot{Z} + \omega_c^2 Z + K'X^2 = z(t) \cos \omega_c t \quad (12)$$

and we have now

$$\omega_c = 2\omega_a. \quad (13)$$

This case is implemented in Josephson circuits as a dc-SQUID whose flux is driven by a microwave oscillating signal at twice the plasma frequency of the SQUID¹⁴. When $z(t) = z_d \gg K'X^2$ (so-called ‘‘stiff’’ or ‘‘non-depleted’’ pump condition), the system of equations (11,12) reduces to the parametrically driven oscillator equation

$$\ddot{X} + \gamma_a \dot{X} + \omega_a^2 \left[1 + \frac{K'z_d}{\gamma_c \omega_c} \sin(\omega_c t) \right] X = x(t) \cos \omega_a t. \quad (14)$$

Note that there is, in addition to the parametric drive on the left hand side, a small perturbing drive signal $x(t) \cos \omega_a t$ on the right hand side. The theory of the degenerate parametric amplifier starts with this latter

equation, the term $\frac{K'z_d}{\gamma_c \omega_c} \sin(\omega_c t)$ corresponding to the pump and $x(t) \cos \omega_a t$ corresponding to the input signal. The output signal is obtained from a combination of the loss term $\gamma_a \dot{X}$ and the input signal.

In the context of Josephson devices, another route to the effective parametric oscillator of equation (14) can be obtained by a driven, Duffing-type oscillator^{15,16}. This system (Josephson bifurcation amplifier) has only one spatial mode and quartic non-linearity,

$$\ddot{X} + \gamma_a \dot{X} + \omega_a^2 X - \lambda X^3 = [z_d + x(t)] \cos \omega_d t. \quad (15)$$

Driven by a strong tone $z_d \cos \omega_d t$ in the vicinity of the bifurcation occurring at

$$\omega_d = \omega_a - \frac{\sqrt{3}}{2} \gamma_a, \quad (16)$$

$$z_d = \frac{128}{27} \sqrt{\frac{\gamma_a^3 \omega_a}{3\lambda}}, \quad (17)$$

it will lead to an equation of the form (14) for small deviations around the steady-state solution. It will, therefore, amplify the small drive modulation signal $x(t)$ of equation (15) [17]. Similar amplifying effects can be found in pumped superconducting microwave resonators without Josephson junctions¹⁸⁻²⁰.

In the following section, we will treat Eqs. (2-4) using input-output theory²¹ and obtain the quantum-mechanical scattering matrix of the signal and idler amplitudes in the stiff-pump approximation. This allows us to find the photon gain of the device in its photon amplifier mode as a function of the pump amplitude, and the corresponding reduction of bandwidth. We then discuss the implementation of the device using a ring of four Josephson junctions flux-biased at half-quantum in Sec. II. It is the non-dissipative analogue of the semiconductor diode ring modulator²². In Sec. III, we treat the finite amplitude of signals and establish useful relations between the dynamic range, gain and bandwidth. In Sec. IV we introduce the Josephson parametric converter (JPC) as an example of a non-degenerate, three-wave mixing device operating at the quantum limit. We present three different realizations schemes for the JPC and point out their practical advantages and limitations. In Sec. V we present experimental results for different JPC devices and compare the data with the maximum bounds predicted by theory. We follow this with a discussion, in Sec. VI, of general requirements for an amplifier

to meet the needs of qubit readout and how the maximum input power of the device can be increased by two orders of magnitude beyond typical values achieved nowadays. We conclude with a brief summary of our results in Sec. VII.

I. INPUT-OUTPUT TREATMENT OF A GENERIC NON-DEGENERATE, THREE-WAVE MIXING DEVICE

The three oscillators of Eqs. (2-4) correspond to three quantum LC oscillators coupled by a non-linear, trilinear mutual inductance, whose mechanism we will discuss in the next section. They are fed by transmission lines which carry excitations both into and out of the oscillators, as shown on Fig. 1. The Hamiltonian of the system is (leaving out the transmission lines for the moment),

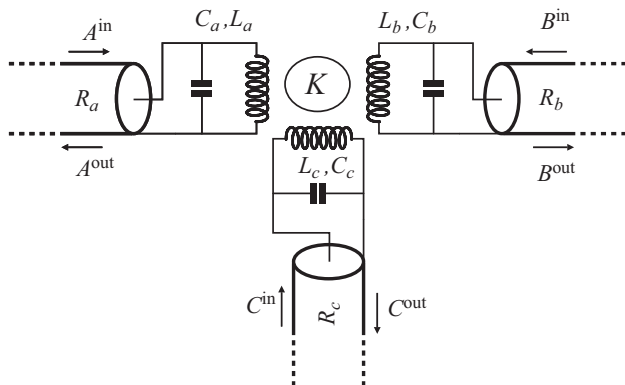


FIG. 1: General non-degenerate three-wave mixing device consisting of three LC oscillators coupled by a non-linear medium, giving a trilinear term in the Hamiltonian of the form $K\Phi_a\Phi_b\Phi_c$ where the fluxes $\Phi_{a,b,c}$ are those of the inductors. Each oscillator is fed by a transmission line with characteristic impedance $R_{a,b,c}$.

$$\frac{H_0}{\hbar} = \omega_a a^\dagger a + \omega_b b^\dagger b + \omega_c c^\dagger c + g_3 (a + a^\dagger)(b + b^\dagger)(c + c^\dagger), \quad (18)$$

where a , b and c are the annihilation operators associated with each of the three degrees of freedom. Their associated angular frequencies are given in terms of the inductances and capacitances as

$$\omega_{a,b,c} = \frac{1}{\sqrt{L_{a,b,c}C_{a,b,c}}}. \quad (19)$$

The bosonic operators of different modes (a , b , c) commute with each other and those associated with the same mode satisfy the usual commutation relations of the form

$$[a, a^\dagger] = 1. \quad (20)$$

The link between the mode amplitude such as X , which represents the flux through the inductance of the oscillator, and a quantum operator such as a can be written as,

$$X = X^{ZPF} (a + a^\dagger), \quad (21)$$

where “ZPF” stands for “zero-point fluctuations” and

$$X^{ZPF} = \sqrt{\frac{\hbar Z_a}{2}}, \quad (22)$$

$$Z_a = \sqrt{\frac{L_a}{C_a}}, \quad (23)$$

the last equation defining the impedance of the oscillator, equal to the modulus of the impedance on resonance of either the inductance or the capacitance. The link between K and g_3 is therefore

$$\hbar g_3 = K X^{ZPF} Y^{ZPF} Z^{ZPF}. \quad (24)$$

We now work in the framework of Rotating Wave Approximation (RWA), in which we only keep terms commuting with the total photon number

$$\frac{H_0^{\text{RWA}}}{\hbar} = \omega_a a^\dagger a + \omega_b b^\dagger b + \omega_c c^\dagger c + g_3 (a^\dagger b^\dagger c + abc^\dagger). \quad (25)$$

Treating in RWA the coupling of each oscillator with a transmission line carrying waves in and out of the oscillator (see Appendix for complements of the next 6 equations), one arrives at three coupled quantum Langevin equations for $a(t)$, $b(t)$ and $c(t)$:

$$\begin{aligned} \frac{d}{dt} a &= -i\omega_a a - ig_3 b^\dagger c - \frac{\gamma_a}{2} a + \sqrt{\gamma_a} \tilde{a}^{\text{in}}(t), \\ \frac{d}{dt} b &= -i\omega_b b - ig_3 a^\dagger c - \frac{\gamma_b}{2} b + \sqrt{\gamma_b} \tilde{b}^{\text{in}}(t), \\ \frac{d}{dt} c &= -i\omega_c c - ig_3 ab - \frac{\gamma_c}{2} c + \sqrt{\gamma_c} \tilde{c}^{\text{in}}(t), \end{aligned} \quad (26)$$

In these equations, the second term in the right hand side corresponds to the non-linear term producing photon conversion. The third term says that photons introduced in one resonator leave with a rate

$$\gamma_{a,b,c} = \omega_{a,b,c} \frac{Z_{a,b,c}}{R_{a,b,c}}, \quad (27)$$

with the resistances $R_{a,b,c}$ denoting the characteristic impedances of the transmission lines. Finally, in the fourth term of the Langevin equations, the input fields such as $\tilde{a}^{\text{in}}(t)$ correspond to the negative frequency component of the drive terms in the classical equations. They obey the relation

$$\tilde{a}^{\text{in}}(t) = \frac{1}{\sqrt{2\pi}} \int_0^{+\infty} a^{\text{in}}[\omega] e^{-i\omega t} d\omega, \quad (28)$$

where $a^{\text{in}}[\omega]$ are the usual field operators obeying the commutation relations

$$[a^{\text{in}}[\omega], a^{\text{in}}[\omega']] = \text{sgn}\left(\frac{\omega - \omega'}{2}\right) \delta(\omega + \omega') \quad (29)$$

in which ω denotes a frequency that can be either positive or negative. The transmission lines thus both damp and drive the oscillators. The incoming field operator treats the drive signals and the Nyquist equilibrium noise of the reservoir on the same footing. Photon spectral densities $\mathcal{N}^{\text{in}}[\omega]$ of the incoming fields, introduced by relations of the form

$$\langle \{a^{\text{in}}[\omega], a^{\text{in}}[\omega']\} \rangle = 2\mathcal{N}_a^{\text{in}} \left[\frac{\omega - \omega'}{2} \right] \delta(\omega + \omega'), \quad (30)$$

have the value

$$\mathcal{N}_a^{\text{in}}[\omega] = \frac{\text{sgn}(\omega)}{2} \coth\left(\frac{\hbar\omega}{2k_B T}\right) + 2\pi P_a^{\text{in}} [\delta(\omega - \omega_1) + \delta(\omega + \omega_1)], \quad (31)$$

where P_a^{in} is the photon flux of the incoming drive signal at angular frequency ω_1 (in units of photons per unit time) and T is the temperature of the electromagnetic excitations of the line. Note that the dimensionless function $\mathcal{N}_a^{\text{in}}[\omega]$ is defined for both positive and negative frequencies. It is symmetric $\mathcal{N}_a^{\text{in}}[\omega] = \mathcal{N}_a^{\text{in}}[-\omega]$ and its value at frequency $|\omega|$ represents the average number of photons per unit time per unit bandwidth in the incoming signal, which in the high temperature limit is $k_B T / (\hbar|\omega|)$. It includes the $\frac{1}{2}$ contribution of zero-point quantum noise.

It is worth insisting that we treat the non-linear coupling strength as a perturbation compared with the influence of the reservoirs, treated themselves as a perturbation compared with the Hamiltonian of the oscillators:

$$g_3 \ll \gamma_a, \gamma_b < \gamma_c \ll \omega_a, \omega_b < \omega_c = \omega_a + \omega_b. \quad (32)$$

In general, only one strong drive tone is applied to one of the resonators and is called the ‘‘pump’’. Two cases must then be distinguished at this stage, as shown in Fig. 2:

Case 1 (amplification and frequency conversion with photon gain): the pump tone is applied to the c resonator. The device is usually used as an amplifier^{4,12}. It can also be used as a two-mode squeezer²³.

Case 2 (noiseless frequency conversion without photon gain): the pump tone is applied to either the a or b resonator²⁴. The device is useful as a noiseless up- and down-converter and can perform dynamical cooling of the lowest energy oscillator, transferring its spurious excitations to the highest frequency one, which is more easily void of any excitations and plays the role of a cold source.

A. Photon gain (case 1)

We will first suppose that the pump is ‘‘stiff’’, namely

$$|\langle \tilde{c}^{\text{in}} \rangle|^2 \gg 1 \quad (33)$$

$$\gamma_c \gg \gamma_a, \gamma_b \quad (34)$$

This means that the pump tone will not be easily depleted despite the fact that its photons are converted into

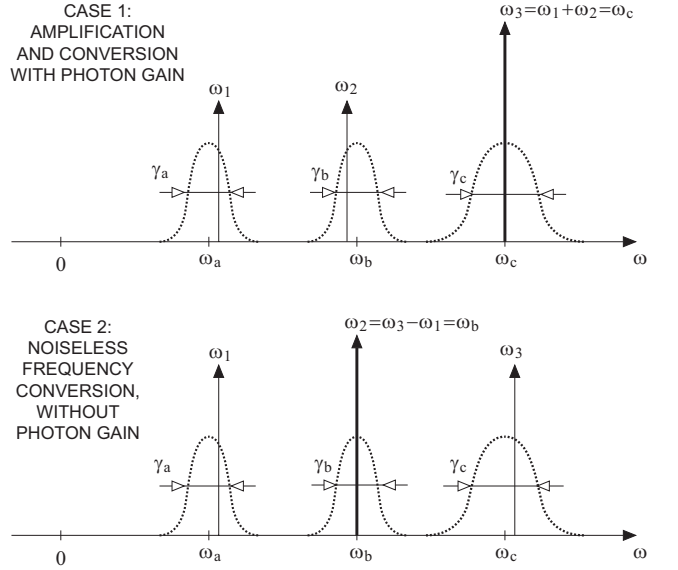


FIG. 2: Characteristic frequency landscape of non-degenerate three-wave mixing devices. Three separate oscillators have resonant frequencies $\omega_a < \omega_b < \omega_c = \omega_a + \omega_b$. They are fed by transmission lines, giving them a full linewidth at half-maximum γ_a , γ_b and γ_c respectively. The non-linear coupling strength, expressed in photon amplitude language, is much smaller than these linewidths. The device can be pumped at ω_c and operates then as a phase-preserving amplifier with photon gain for frequencies ω_a and ω_b (top), or it can be pumped at one of the two lower frequencies ω_a or ω_b and operates then as a noiseless frequency converter or dynamical cooler, upconverting signals into oscillator at ω_c (bottom). In this figure, the spectral density of weak signal corresponds to thin arrows whereas the spectral densities of pump signals corresponds to thick arrows.

the signal and idler photons at ω_a and ω_b . For solving the quantum Langevin equations, we replace the pumped oscillator annihilation operator c by its average value in the coherent state produced by the pump as

$$c(t) \rightarrow \langle c(t) \rangle = \sqrt{\bar{n}_c} e^{-i(\omega_c t + \phi)}. \quad (35)$$

The Langevin equations can then be transformed into the linear equations (see equation (178) of Appendix)

$$\begin{bmatrix} O_a^+ & ig_b^a e^{-i\omega_c t} \\ -ig_a^{b*} e^{+i\omega_c t} & O_b^{+*} \end{bmatrix} \begin{bmatrix} \tilde{a}^{\text{out}} \\ \tilde{b}^{\text{out}\dagger} \end{bmatrix} = - \begin{bmatrix} O_a^- & ig_b^a e^{-i\omega_c t} \\ -ig_a^{b*} e^{+i\omega_c t} & O_b^{-*} \end{bmatrix} \begin{bmatrix} \tilde{a}^{\text{in}} \\ \tilde{b}^{\text{in}\dagger} \end{bmatrix}, \quad (36)$$

where

$$O_{a,b}^{\pm} = \frac{d}{dt} + i(\omega_{a,b} \mp i\Gamma_{a,b}), \quad (37)$$

$$\Gamma_{a,b} = \frac{\gamma_{a,b}}{2}, \quad (38)$$

$$g_{b,a}^{a,b} = g_3 \sqrt{\bar{n}_c} e^{-i\phi} \sqrt{\frac{\Gamma_{a,b}}{\Gamma_{b,a}}}. \quad (39)$$

After a Fourier transform, we obtain in the frequency domain, a simpler relation

$$\begin{bmatrix} h_a[\omega_1] & +ig_b^a \\ -ig_a^{b*} & h_b^*[\omega_2] \end{bmatrix} \begin{bmatrix} a^{\text{out}}[+\omega_1] \\ b^{\text{out}}[-\omega_2] \end{bmatrix} = \begin{bmatrix} h_a^*[\omega_1] & -ig_b^a \\ +ig_a^{b*} & h_b[\omega_2] \end{bmatrix} \begin{bmatrix} a^{\text{in}}[+\omega_1] \\ b^{\text{in}}[-\omega_2] \end{bmatrix}, \quad (40)$$

where

$$h_{a,b}[\omega] = -i\omega + i(\omega_{a,b} - i\Gamma_{a,b}) \quad (41)$$

and the signal and idler angular frequencies ω_1 and ω_2 are both positive, satisfying the relationship

$$\omega_1 + \omega_2 = \omega_c. \quad (42)$$

The scattering matrix of the device for small signals is defined by

$$\begin{bmatrix} a^{\text{out}}[+\omega_1] \\ b^{\text{out}}[-\omega_2] \end{bmatrix} = \begin{bmatrix} r_{aa} & s_{ab} \\ s_{ba} & r_{bb} \end{bmatrix} \begin{bmatrix} a^{\text{in}}[+\omega_1] \\ b^{\text{in}}[-\omega_2] \end{bmatrix}. \quad (43)$$

It can be computed from Eq. (40) and one finds

$$r_{aa} = \frac{\chi_a^{-1*} \chi_b^{-1*} + |\rho|^2}{\chi_a^{-1} \chi_b^{-1*} - |\rho|^2}, \quad (44)$$

$$r_{bb} = \frac{\chi_a^{-1} \chi_b^{-1} + |\rho|^2}{\chi_a^{-1} \chi_b^{-1*} - |\rho|^2}, \quad (45)$$

$$s_{ab} = \frac{-2i\rho}{\chi_a^{-1} \chi_b^{-1*} - |\rho|^2}, \quad (46)$$

$$s_{ba} = \frac{2i\rho^*}{\chi_a^{-1} \chi_b^{-1*} - |\rho|^2}, \quad (47)$$

where the χ 's are the bare response functions of modes a and b (whose inverses depend linearly on the signal frequency)

$$\chi_a^{-1} = 1 - i \frac{\omega_1 - \omega_a}{\Gamma_a}, \quad (48)$$

$$\chi_b^{-1} = 1 - i \frac{\omega_2 - \omega_b}{\Gamma_b}, \quad (49)$$

and ρ is the dimensionless pump amplitude

$$\rho = \frac{g_3 \sqrt{\bar{n}_c} e^{-i\phi}}{\sqrt{\Gamma_a \Gamma_b}}. \quad (50)$$

Note that the matrix in Eq. (43) has unity determinant and the property

$$|r_{aa}|^2 - |s_{ab}|^2 = 1, \quad (51)$$

$$|r_{bb}|^2 - |s_{ba}|^2 = 1. \quad (52)$$

For zero frequency detuning, i.e. $\chi_a^{-1} = \chi_b^{-1} = 1$, the scattering matrix displays a very simple form

$$\begin{bmatrix} \cosh \tau_0 & -ie^{-i\phi} \sinh \tau_0 \\ +ie^{+i\phi} \sinh \tau_0 & \cosh \tau_0 \end{bmatrix}, \quad (53)$$

where $\tanh(\tau_0/2) = |\rho|$. The zero frequency detuning power gain G_0 is given by

$$G_0 = (\cosh \tau_0)^2 = \left(\frac{1 + |\rho|^2}{1 - |\rho|^2} \right)^2. \quad (54)$$

For non-zero detuning, the scattering matrix acquires extra phase factors but the minimal scattering matrix for a quantum-limited phase-preserving amplifier represented in Fig. 3 still describes the device. The gain G_0

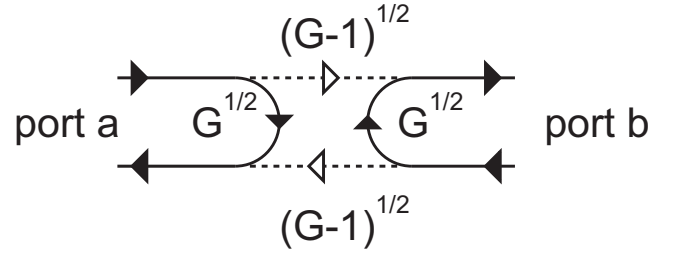


FIG. 3: An amplifier reaching the quantum limit must have a minimal scattering matrix, with the signal in port a being reflected with amplitude gain $G^{1/2}$ while the signal in port b is phase-conjugated and transmitted to port a with amplitude gain $(G-1)^{1/2}$. This can be realized in case 1 of Fig. 2.

diverges as $|\rho| \rightarrow 1^-$, i.e. when the photon number \bar{n}_c in the pump resonator reaches the critical number given by

$$\bar{n}_c^{po} = \frac{\Gamma_a \Gamma_b}{|g_3|^2}, \quad (55)$$

a result that is common to all forms of parametric amplification. Increasing the pump power beyond the critical power yielding \bar{n}_c^{po} leads to the parametric oscillation regime. This phenomenon is beyond the scope of our simple analysis and cannot be described by our starting equations, since higher order non-linearities of the system need to be precisely modelled if the saturation of the oscillation is to be accounted for.

Introducing the detuning

$$\Delta\omega = \omega_1 - \omega_a = \omega_b - \omega_2, \quad (56)$$

we can give a useful expression for the gain as a function of frequency as

$$G(\Delta\omega) \Big|_{|\rho| \rightarrow 1^-} = \frac{G_0}{1 + \left(\frac{\Delta\omega}{\gamma G_0^{-1/2}}\right)^2}, \quad (57)$$

which shows that in the limit of large gain, the response of the amplifier for both the signal and idler port is Lorentzian with a bandwidth given by

$$B = 2\gamma G_0^{-1/2} = \frac{2\gamma_a \gamma_b G_0^{-1/2}}{\gamma_a + \gamma_b}. \quad (58)$$

The product of the maximal amplitude gain times the bandwidth is thus constant and is given by the harmonic average of the oscillator bandwidths. Another interesting prediction of the scattering matrix is the two-mode squeezing function of the device demonstrated in Ref. 25.

B. Conversion without photon gain (case 2)

The case of conversion without photon gain can be treated along the same line as in the previous subsection, where scattering takes place between c and a or c and b modes. Without loss of generality we assume that the pump is applied to the intermediate frequency resonance. In this case the scattering matrix reads

$$\begin{bmatrix} a^{\text{out}}[+\omega_1] \\ c^{\text{out}}[+\omega_3] \end{bmatrix} = \begin{bmatrix} r_{aa} & t_{ac} \\ t_{ca} & r_{cc} \end{bmatrix} \begin{bmatrix} a^{\text{in}}[+\omega_1] \\ c^{\text{in}}[+\omega_3] \end{bmatrix}, \quad (59)$$

where

$$\begin{aligned} r_{aa} &= \frac{\chi_a^{-1*} \chi_c^{-1} - |\rho'|^2}{\chi_a^{-1} \chi_c^{-1} + |\rho'|^2}, \\ r_{cc} &= \frac{\chi_a^{-1} \chi_c^{-1*} - |\rho'|^2}{\chi_a^{-1} \chi_c^{-1} + |\rho'|^2}, \\ t_{ac} &= \frac{2i\rho'}{\chi_a^{-1} \chi_c^{-1} + |\rho'|^2}, \\ t_{ca} &= \frac{2i\rho'^*}{\chi_a^{-1} \chi_c^{-1} + |\rho'|^2}, \end{aligned} \quad (60)$$

and

$$\chi_c^{-1} = 1 - i \frac{\omega_3 - \omega_c}{\Gamma_c}, \quad (61)$$

$$\rho' = \frac{g_3 \sqrt{\bar{n}_b} e^{-i\phi}}{\sqrt{\Gamma_a \Gamma_c}}. \quad (62)$$

The reduced pump strength ρ' plays the same role here as ρ in the photon amplification case. Note that the

scattering matrix is now unitary (conservation of total number of photons) and satisfies the following relations:

$$|r_{aa}|^2 + |t_{ac}|^2 = 1, \quad (63)$$

$$|r_{cc}|^2 + |t_{ca}|^2 = 1. \quad (64)$$

For zero frequency detuning, i.e. $\chi_a^{-1} = \chi_c^{-1} = 1$, the scattering matrix can be written as

$$\begin{bmatrix} \cos \tau_0 & e^{-i\phi} \sin \tau_0 \\ e^{i\phi} \sin \tau_0 & \cos \tau_0 \end{bmatrix}, \quad (65)$$

which corresponds to replacing the parameter τ_0 by $i\tau_0$ or $|\rho|$ by $i|\rho|$ in the scattering matrix (53). A scattering representation of the two-port device in conversion mode is shown in Fig. 4. In this mode the device operates as a beam splitter, the only difference being that the photons in different arms have different frequencies²⁴. Full conversion ($\sin \tau_0 = 1$) is obtained on resonance when the pump power reaches the critical value. However, here, the critical value can be traversed without violating the validity of the equations. Full photon conversion is desirable in dynamical cooling: in that case, the higher frequency resonator will be emptied of photons, and the lower frequency resonator can be cooled to its ground state by pumping the intermediate frequency resonator (see lower panel of Fig. 2).

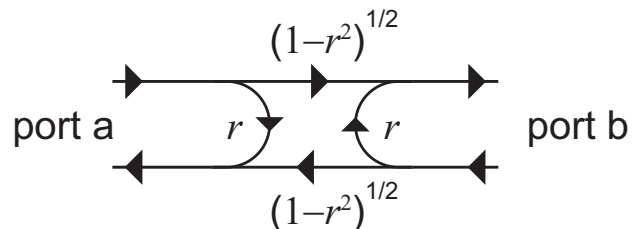


FIG. 4: Signal flow graph for a three-wave mixing device operating in conversion without photon gain, realized in case 2 of Fig. 2. The incoming signal in port a (b) is reflected with amplitude r and transmitted with up-conversion (down-conversion) to port b (a) with amplitude $(1 - r^2)^{1/2}$.

C. Added Noise

The number of output photons generated per mode in the amplification (case 1) is given by

$$\mathcal{N}_{a,b}^{\text{out}} = |r|^2 \mathcal{N}_{a,b}^{\text{in}} + |s|^2 \mathcal{N}_{b,a}^{\text{in}}, \quad (66)$$

where \mathcal{N}^{in} is the input photon spectral density given by Eq. (31) and we assume that there is no cross-correlations between the input fields a^{in} and b^{in} .

Assuming that the three-wave mixing device is in thermal equilibrium at temperature $T \ll \hbar\omega_{1,2}/k_B$ and that the dominant noise entering the system at each port is zero-point fluctuations $\hbar\omega_{1,2}/2$ ($\mathcal{N}^{\text{in}} = 1/2$), then in the limit of high gain $|r| \gg 1$, the number of noise equivalent photons effectively feeding the system is

$$\mathcal{N}_{eq}^{\text{in}} = \mathcal{N}^{\text{out}} / |r|^2 \simeq 1. \quad (67)$$

This means that the number of noise equivalent photons added by the device to the input is given by $\mathcal{N}^{\text{add}} = \mathcal{N}_{eq}^{\text{in}} - \mathcal{N}^{\text{in}} = 1/2$. Hence, when operated as a non-degenerate amplifier with $G_0 \gg 1$, the device adds noise which is equivalent to at least half a photon at the signal frequency to the input, in agreement with Caves theorem²⁶.

In contrast, in the conversion mode of operation, assuming that there is no correlation between the input fields, the number of generated output photons per mode reads

$$\mathcal{N}_{a,b}^{\text{out}} = |r|^2 \mathcal{N}_{a,b}^{\text{in}} + |t|^2 \mathcal{N}_{b,a}^{\text{in}}. \quad (68)$$

Therefore, in pure conversion where $|r| = 0$ and $|t| = 1$, when referring the noise back to the input, one gets noise equivalent photons

$$\mathcal{N}_{eq}^{\text{in}} = \mathcal{N}^{\text{out}} / |t|^2 = 1/2. \quad (69)$$

This means that, as a converter, the device is not required to add noise to the input since $\mathcal{N}_{eq}^{\text{in}} = \mathcal{N}^{\text{in}}$.

II. THREE-WAVE MIXING USING JRM

The Josephson ring modulator is a device consisting of four Josephson junctions, each with critical current $I_0 = \frac{\hbar}{2eL_J}$ forming a ring threaded by a flux $\Phi = \Phi_0/2$ where Φ_0 is the flux quantum (see Fig. 5). The device has the symmetry of a Wheatstone bridge. There are thus three orthogonal electrical modes coupled to the junctions, corresponding to the currents I_X , I_Y and I_Z flowing in three external inductances L_X , L_Y and L_Z that are much larger than the junction inductance $L_J = \varphi_0^2 E_J^{-1}$, where $\varphi_0 = \hbar/2e$ is the reduced flux quantum. Each junction $j \in \{\alpha, \beta, \gamma, \delta\}$ is traversed by a current I_j and at the working point (i.e. $\Phi = \Phi_0/2$) its energy is, keeping terms up to order four in I_j , given by

$$E_j = \frac{1}{2} L_J^{\text{eff}} I_j^2 - \frac{1}{24} \frac{L_J^{\text{eff}}}{I_0^2} I_j^4, \quad (70)$$

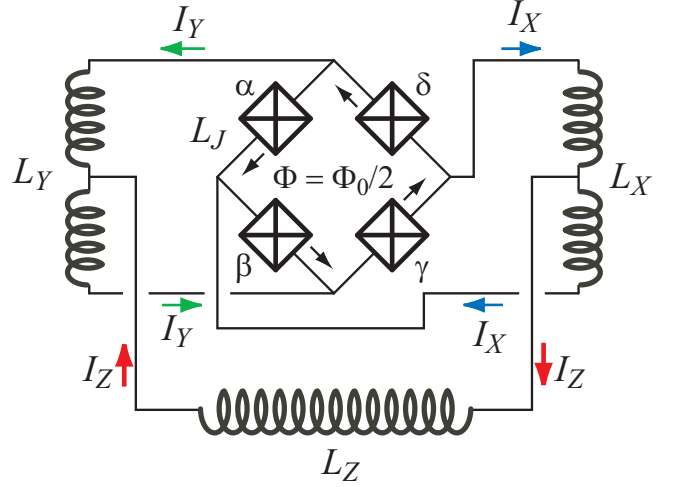


FIG. 5: Three-wave mixing element (see ellipse marked K in Fig. 1) consisting of a loop of four nominally identical Josephson junctions threaded by a flux in the vicinity of half a flux quantum. Mutual inductances, not shown here, couple this circuit to inductances L_a , L_b and L_c of Fig. 1 via the inductances L_X , L_Y and L_Z respectively, which are much larger than the junction inductance L_J . The three currents I_X , I_Y and I_Z correspond to the three orthogonal modes of the structure.

where $L_J^{\text{eff}} = \sqrt{2}L_J$ and $I_0' = I_0/\sqrt{2}$. The currents in the junctions are expressed by

$$I_\alpha = \frac{-I_X - I_Y}{2} + \frac{I_Z}{4} + I_\Phi, \quad (71)$$

$$I_\beta = \frac{+I_X - I_Y}{2} - \frac{I_Z}{4} + I_\Phi, \quad (72)$$

$$I_\gamma = \frac{+I_X + I_Y}{2} + \frac{I_Z}{4} + I_\Phi, \quad (73)$$

$$I_\delta = \frac{-I_X + I_Y}{2} - \frac{I_Z}{4} + I_\Phi, \quad (74)$$

where I_Φ is the supercurrent induced in the ring by the externally applied flux Φ . The total energy of the ring is, keeping terms up to third order in the currents²⁷,

$$E_{\text{ring}} = \frac{1}{2} L_J^{\text{eff}} \left(I_X^2 + I_Y^2 + \frac{1}{4} I_Z^2 \right) - \frac{1}{4} \frac{L_J^{\text{eff}} I_\Phi}{I_0'^2} I_X I_Y I_Z. \quad (75)$$

We can express the currents as

$$I_{X,Y,Z} = \frac{\Phi_{a,b,c}}{L_{a,b,c}} \frac{M_{a,b,c}}{L_{X,Y,Z}} = \frac{\Phi_{a,b,c}}{L_{a,b,c}^{\text{eff}}}, \quad (76)$$

where $M_{a,b,c}$ are the mutual inductances between $L_{X,Y,Z}$ and the oscillator inductances $L_{a,b,c}$. The non-linear coefficient in the energy is, therefore,

$$K = \frac{(L_J^{\text{eff}})^2}{4\varphi_0} \frac{1}{L_a^{\text{eff}} L_b^{\text{eff}} L_c^{\text{eff}}}, \quad (77)$$

and we finally arrive at the result

$$g_3^2 = \frac{p_a p_b p_c \omega_a \omega_b \omega_c}{\omega_J^{eff}}. \quad (78)$$

Here the participation ratios are defined as

$$p_{a,b,c} = \frac{L_J^{eff}}{L_{a,b,c}^{eff}}, \quad (79)$$

and, at $\Phi = \Phi_0/2$,

$$\omega_J^{eff} = \frac{128 E_J}{\sqrt{2} \hbar}. \quad (80)$$

The participation ratios are linked to the maximal number of photons in each resonator, defined as those corresponding to an oscillation amplitude reaching a current of I_0 in each junction of the ring modulator,

$$p_{a,b,c} \bar{n}_{a,b,c}^{\max} = \frac{E_J^{a,b,c}}{\hbar \omega_{a,b,c}}, \quad (81)$$

where the $E_J^{a,b,c}$ are of order E_J with factors accounting for the different participation of modes X , Y and Z in the current of each junction. Equations (78) and (81) are valid for all types of coupling between the Josephson ring modulator and signal/pump oscillators, which can be realized in practice by inductance sharing rather than by the mutual inductances discussed here.

Equation (81) can also be rewritten in terms of the maximum circulating power in cavities a and b as

$$P_{\text{cav}}^{\max} = \frac{\gamma_{a,b} E_J}{p_{a,b} \sqrt{2}} \quad (82)$$

where we substituted $E_J/\sqrt{2}$ as an upper bound for $E_J^{a,b}$. The maximum number of photons in equation (81) determine the maximum signal input power handled by the device

$$P_{a,b}^{\max} = \frac{1}{G} \gamma_{a,b} \hbar \omega_{a,b} \bar{n}_{a,b}^{\max}. \quad (83)$$

We can now combine the notion of maximum power in resonator c compatible with weak non-linearity with that of a critical power for the onset of parametric oscillation given by Eq. (55):

$$\bar{n}_c^{\max} = \frac{E_J^c}{p_c \hbar \omega_c} > \bar{n}_c^{\text{po}} = \frac{\Gamma_1 \Gamma_2}{g_3^2}, \quad (84)$$

arriving at the important relation

$$p_a p_b Q_a Q_b > \Xi, \quad (85)$$

where Ξ is a number of order unity depending on the exact implementation of the coupling between the ring

Parameter	Range
$\omega_{a,b}/2\pi$	1 - 16 GHz
$Q_{a,b}$	50 - 500
$Z_{a,b}$	10 - 150 Ω
γ_c	0.5 - 10 GHz
I_0	0.5 - 10 μ A
E_J	10 - 230 K
$p_{a,b,c}$	0.01 - 0.5
$g_3/2\pi$	0.1 - 15 MHz
$\bar{n}_{a,b,c}^{\max}$	20 - 10^4

TABLE II: Typical values for Josephson three-wave mixing devices.

modulator and the oscillators. The quality factors of the resonators obey the well-known relation

$$Q_{a,b} = \frac{\omega_{a,b}}{\gamma_{a,b}}. \quad (86)$$

Another maximum limit on the gain of the amplifier is set by the saturation of the device due to amplified zero-point fluctuations present at the input given by

$$G_{\text{ZPF}}^{\max} = \frac{E_J}{\sqrt{2} p_{a,b} \hbar \omega_{a,b}} \cdot 2. \quad (87)$$

Eqs. (81), (83) and (85) show that it is not possible to maximize simultaneously gain, bandwidth and dynamic range.

In table II we enlist general bounds on the characteristic parameters of the three-wave mixing device, which are feasible with superconducting microwave circuits and standard Al-AlOx-Al junction fabrication technology. A few comments regarding the values listed in the table are in order. The frequency ranges of resonators a and b is mainly set by the center frequency of the system whose signal one needs to amplify or process. It is also important that these frequencies are very small compared to the plasma frequency of the Josephson junction. The total quality factor range listed in the table (50 - 500) is suitable for practical devices. Quality factors in excess of 500 can be easily achieved with superconducting resonators but, as seen from Eq. (58), higher the quality factor, smaller the dynamical bandwidth of the device. Quality factors lower than 50 on the other hand are not recommended either for a variety of reasons. For example, in the limit of very low Q the pump softens (becomes less stiff), and the dynamic range decreases as more quantum noise will be admitted by the device bandwidth and amplified “unintentionally” by the junctions. The characteristic impedance of the resonators $Z_{a,b}$ is set by microwave engineering considerations as discussed in Sec. IV but, in general, this value varies around 50 Ω . The rate γ_c at which pump photons leave the circuit varies from one circuit design to the other as discussed

in Sec. IV and is limited by ω_c . This parameter also affects the maximum input power performance of the device as explained in Sec. III. As to the values of I_0 , on the one hand it is beneficial to work with large Josephson junctions in order to increase the processing capability of the device; on the other hand a critical current larger than $10 \mu\text{A}$ adds complexity to the microwave design of the resonators and makes the fabrication process of the Josephson junction more involved. This might even require switching to a different fabrication process such as Nb-AlOx-Nb trilayer junctions²⁸ or nanobridges²⁹. The other parameters listed in the table, namely $p_{a,b,c}$, E_J , g_3 , $\bar{n}_{a,b,c}^{\text{max}}$, their values depend, to a large extent, on the device parameters already discussed.

III. LIMITATION OF DYNAMIC RANGE DUE TO PUMP DEPLETION

In the last two sections, we were using results obtained by solving only the first two of the equations of motion Eqs. (26) under the restriction of the stiff pump approximation. In this section, we extend our analysis and include the third equation describing the dynamics of the pump to calculate the pump depletion and its effect on the dynamic range of the device. For this purpose, we consider the average value of the third equation of motion for field c

$$\frac{d}{dt} \langle c \rangle = -i\omega_c \langle c \rangle - ig_3 \langle ab \rangle - \frac{\gamma_c}{2} \langle c \rangle + \sqrt{\gamma_c} \langle \tilde{c}^{\text{in}}(t) \rangle. \quad (88)$$

In steady state and using RWA we obtain

$$ig_3 \langle ab \rangle + \frac{\gamma_c}{2} \langle c(t) \rangle = \sqrt{\gamma_c} \langle \tilde{c}^{\text{in}}(t) \rangle. \quad (89)$$

In the limit of vanishing input, the cross-correlation term $\langle ab \rangle$ is negligible and, therefore,

$$\langle c(t) \rangle = \frac{2}{\sqrt{\gamma_c}} \langle \tilde{c}^{\text{in}}(t) \rangle. \quad (90)$$

The average number of photons in the c resonator in this case is, thus,

$$\lim_{\langle ab \rangle \rightarrow 0} \bar{n}_c = \frac{4}{\gamma_c} |\langle \tilde{c}^{\text{in}}(t) \rangle|^2. \quad (91)$$

We now establish a self-consistent equation for \bar{n}_c , taking into account input signals of finite amplitude. We first evaluate the value of $\langle a(t)b(t) \rangle$ in the frame rotating with the pump phase,

$$\begin{aligned} & \langle a(t)b(t) \rangle \\ &= \frac{1}{2\pi} \int_{-\infty}^{+\infty} \int_{-\infty}^{+\infty} \langle a[\omega] b[\omega'] \rangle e^{-i(\omega+\omega')t} d\omega d\omega'. \end{aligned} \quad (92)$$

Using the field relations (see Appendix)

$$\sqrt{\gamma_a} a[\omega] = \tilde{a}^{\text{in}}[\omega] + \tilde{a}^{\text{out}}[\omega], \quad (93)$$

$$\sqrt{\gamma_b} b[\omega] = \tilde{b}^{\text{in}}[\omega] + \tilde{b}^{\text{out}}[\omega] \quad (94)$$

and the input-output relations given by Eq. (43), we obtain (transforming back into the time domain)

$$-ig_3 \langle a(t)b(t) \rangle = -\frac{\gamma_{eff}(G)}{2} \langle c(t) \rangle, \quad (95)$$

where, in the limit of large gains $G \gg 1$,

$$\gamma_{eff}(G) = \frac{1}{2\pi} \frac{\gamma_c}{4\bar{n}_c^{\text{in}}} \int_0^{+\infty} d\omega (\mathcal{N}_a^{\text{in}}[\omega] + \mathcal{N}_b^{\text{in}}[\omega]) G(\Delta\omega) \quad (96)$$

denotes an effective decay rate of pump photons due to generation of entangled signal and idler photons. This last relation expresses, in another form, the Manley-Rowe relations³⁰ that establish the equality between the number of created signal photons by the amplifier to the number of destroyed pump photons. It shows that even in the absence of any deterministic signal applied to the oscillator a or b , pump photons are used to amplify zero-point fluctuations. Therefore, the pump tone always encounters a dissipative load even when no signals are injected into the device.

For a continuous wave (CW) input power sent at the center frequency of the a or b oscillator, or both, we have

$$\gamma_{eff}(G_0, P^{\text{in}}) = \frac{\gamma_c}{4\bar{n}_c^{\text{in}}} G_0 P^{\text{in}}, \quad (97)$$

where $P^{\text{in}} = P_a^{\text{in}} + P_b^{\text{in}}$ is given in units of photon number per unit time and, in steady state,

$$\bar{n}_c(G_0, P^{\text{in}}) = \frac{4\gamma_c}{(\gamma_c + \gamma_{eff}(G_0, P^{\text{in}}))^2} \bar{n}_c^{\text{in}}. \quad (98)$$

As a finite input power is applied to the signal oscillators, oscillator c depopulates and, keeping the pump power constant, we get

$$\frac{\bar{n}_c(G_0, P^{\text{in}})}{\bar{n}_c(G_0, P^{\text{in}}=0)} = \frac{1}{\left(1 + \frac{G_0 P^{\text{in}}}{4\bar{n}_c^{\text{in}}}\right)^2} \quad (99)$$

$$\simeq 1 - \frac{G_0 P^{\text{in}}}{2\bar{n}_c^{\text{in}}}. \quad (100)$$

On the other hand, from Eqs. (50) and (54), the left hand side is given by

$$\frac{\bar{n}_c(G_0, P^{\text{in}})}{\bar{n}_c(G_0, P^{\text{in}}=0)} = \frac{\sqrt{G}-1}{\sqrt{G+1}}, \quad (101)$$

where G denotes the gain in the presence of P_{in} . In the large gain limit, if we fix the maximum decrease of gain due to pump depletion to be

$$\frac{G}{G_0} > 1 - \varepsilon \quad (102)$$

with $\varepsilon \ll 1$, then we obtain

$$\frac{P^{\text{in}}}{2\bar{n}_c^{\text{in}}} < \varepsilon G_0^{-3/2}, \quad (103)$$

which can also be rewritten as

$$\frac{2\bar{n}_c^{\text{in}}}{G_0 P_{\text{in}}} > \varepsilon^{-1} \sqrt{G_0}. \quad (104)$$

This relation shows that the ratio of the power of the pump tone to that of the signal at the output of the amplifier must always be much larger than the amplitude gain, in order for the linearity of the amplifier not to be compromised by pump depletion effects.

In Fig. 6 we plot a calculated response of the signal output power P_{out} versus the signal input power P_{in} for a typical three-wave mixing device. The device parameters employed in the calculation and listed in the figure caption are practical values yielding a maximum input power, which is limited by the effect of pump depletion. The different blue curves are obtained by solving Eq. (98) for G and using the input-output relation $P_{\text{out}} = GP_{\text{in}}$, where P_{in} expressed in units of power is taken as the independent variable and G_0 is treated as a parameter. Note that in solving Eq. (98), equations (97), (91), (50) and (54) are used. When drawn on logarithmic scale, the device gain translates into a vertical offset (arrow indicating G_0) off the $P_{\text{out}} = P_{\text{in}}$ line, indicated in red. The dashed black vertical line corresponds to a signal input power of 1 photon at the signal frequency per inverse dynamical bandwidth of the device at $G_0 = 20$ dB. The dashed green line corresponds to the maximum gain set by the amplified zero-point fluctuations given by Eq. (87), while the cyan line corresponds to the maximum circulating power in the cavity given by Eq. (82). Furthermore, the maximum bound $P_{\text{out}}^{\text{max}}$ indicated by the solid magenta line corresponds to $P_{\text{out}}^{\text{max}} = G_0 P_{\text{in}}^{\text{max}}$, where $P_{\text{in}}^{\text{max}} = P_b^{\text{max}}/G_0^{3/2}$ and $P_b^{\text{max}} = P_{\text{cav}}^{\text{max}}$. As can be seen in the figure the predicted power scaling due to pump depletion effect, expressed in relation (103), follows the calculated response quite well. Finally, it is straightforward to see that the usable region in the parameter space of the device with respect to gain, bandwidth and maximum input power lies within the boundaries of the fictitious triangle ABC indicated in the figure which is formed by the intersection of the magenta, black and red lines.

IV. THE JOSEPHSON PARAMETRIC CONVERTER

We discuss here three different realizations of the Josephson parametric converter (JPC), which constitutes a fully non-degenerate three-wave mixing device capable of amplification and conversion as discussed in the previous sections. The three schemes differ in the resonator circuit design and the coupling between the feedline and the resonator.

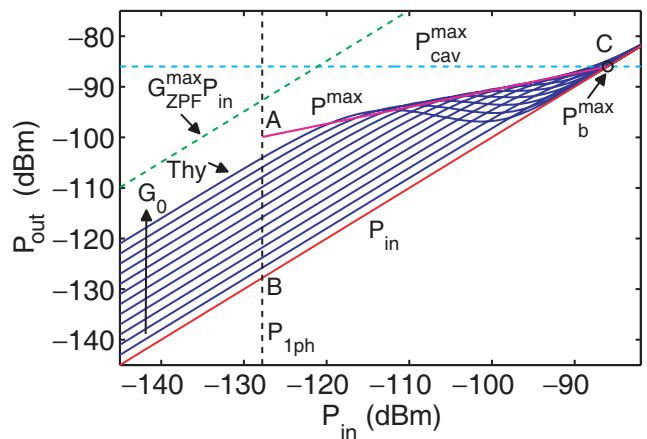


FIG. 6: (Color online). A calculated response of the signal output power P_{out} versus the signal input power P_{in} of a typical three-wave mixing device which exhibits a pump depletion effect. The different blue curves correspond to different G_0 setpoints. The definition of the other lines in the figure is given in the text. The parameters used in the calculation are: $\omega_a/2\pi = 7$ GHz, $\omega_b/2\pi = 8$ GHz, $\omega_c/2\pi = 15$ GHz, $\gamma_a/2\pi = \gamma_b/2\pi = 50$ MHz, $\gamma_c/2\pi = 0.6$ GHz, $Q_a = 140$, $Q_b = 160$, $p_a = p_b = 0.03$, $p_c = 0.02$, $I_0 = 1 \mu\text{A}$, $E_J^{a,b} = E_J/\sqrt{2} = 16.3$ K, $P_{1\text{ph}} = -128$ dBm, $G_{\text{ZPF}}^{\text{max}} = 35$ dB, $P_{\text{cav}}^{\text{max}} = P_b^{\text{max}} = -86$ dBm and $g_3/2\pi = 0.7$ MHz.

A. Microstrip Resonator JPC (MRJ)

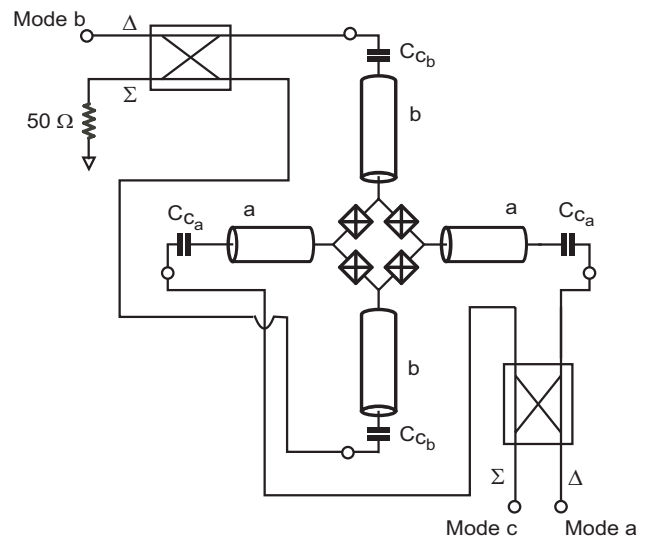


FIG. 7: Circuit model of the Microstrip Resonator JPC (MRJ).

The MRJ comprises two superconducting microstrip resonators which intersect at a JRM at the center as shown in the circuit model of the device in Fig. 7. The

resonance frequencies of the MRJ are determined by the lengths of the microstrips $l_a \simeq \lambda_a/2$ and $l_b \simeq \lambda_b/2$ and the Josephson inductance of the JRM, where λ_a, λ_b are the wavelengths of the fundamental resonances at ω_a and ω_b . It is worth mentioning that in addition to the differential modes a and b , this configuration of two coupled resonators also supports a common (even) mode. The angular frequency ω_e at which this even mode resonates lies between $(\omega_b + \omega_a)/2$ and ω_b (where $\omega_b > \omega_a$). The characteristic impedance of the resonators in the MRJ model is designed to be 50Ω to ensure optimal coupling to the feedlines. Figure 8 exhibits an optical image of a typical MRJ device. The resonators are usually made of Al or Nb over sapphire or high-resistivity silicon and are coupled to the (transmission-line) feedlines using gap capacitors. The main role of these coupling capacitors is to set the external quality factor of the resonators. For a large bandwidth device operating in the 6–10 GHz band, the external Q of the resonators is typically in the range 60–100. In all JPC designs discussed here the total Q essentially coincides with the external Q , since the internal losses of the resonators are less than 10^{-4} . Signals at ω_1 and ω_2 , which lie within the bandwidths of resonators a and b , are fed into the JPC through the delta port of a 180 degree hybrid, whereas the pump drive applied at $\omega_3 = \omega_1 + \omega_2$, for amplification, is a non-resonant tone and is injected into the device through the sigma port of the hybrid (Fig. 7). The main advantage of the MRJ is that it is easy to design and fabricate. On the other hand, the main disadvantages are: (1) the area of the device can be relatively large depending on the frequencies of interest, (2) the characteristic impedance of the device is limited to around 50Ω , (3) the pump can be less stiff than the designs discussed below. The latter is due to the fact that the transmission-line resonators support higher resonance modes such as $2\omega_a$ and $2\omega_b$ with finite Q , which can be relatively close to the pump angular frequency ω_3 .

B. Compact Resonator JPC (CRJ)

In order to mitigate some of the drawbacks of the MRJ, we developed a new JPC design based on compact resonators known as CRJ. The circuit model of the CRJ, shown in Fig. 9, consists of four equal capacitors denoted as C and two pairs of linear inductors connected in series with the JRM whose total inductance is L_a and L_b respectively. Using symmetry considerations one can verify that this circuit has three eigenmodes. Two differential eigenmodes which resonate at bare angular frequencies $\omega_a = 1/\sqrt{(L_a + L_J^{eff})C}$, $\omega_b = 1/\sqrt{(L_b + L_J^{eff})C}$, where L_J^{eff} is the equivalent Josephson inductance of the JRM biased at half a flux quantum, and an even eigenmode which resonates at a lower bare angular frequency $\omega_e = 1/\sqrt{(L_a + L_b + L_J^{eff})C}$. Figure 10 shows an opti-

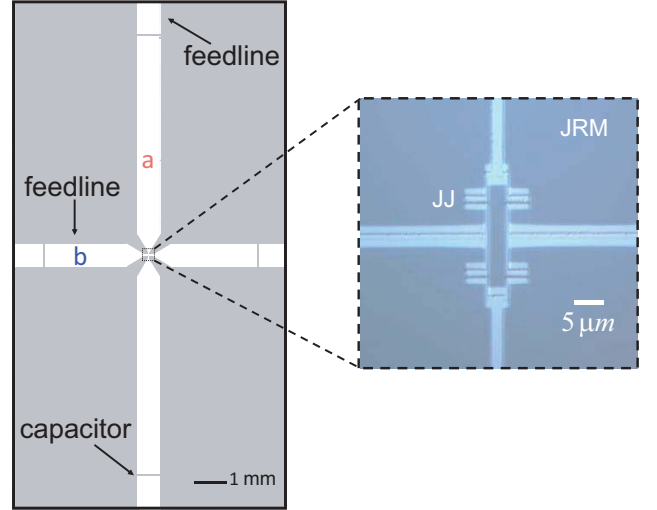


FIG. 8: (Color online). Optical microscope image of a microstrip resonator JPC (MRJ). The resonators denoted a and b are half-wave microstrip resonators which intersect at a JRM. A zoomed-in view of the JRM, which consists of four Josephson junctions arranged in Wheatstone bridge configuration, is shown on the right. The MRJ is coupled to 50Ω feedlines via gap capacitors.

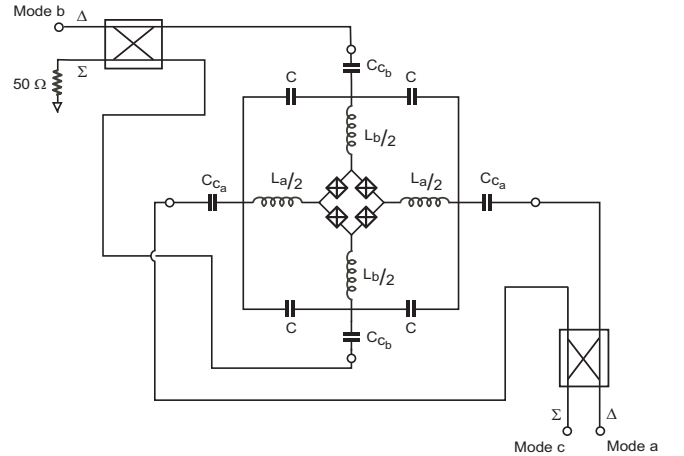


FIG. 9: Circuit model of the Compact Resonator JPC (CRJ).

cal image of a typical compact JPC. The resonators of the device are made of Nb deposited over sapphire substrate. They are fabricated using a standard photolithography step and RIE etching. The JRM at the center of the device is made of Aluminum. It is fabricated using e-beam lithography, and angle shadow evaporation. As can be seen in the figure, the capacitance elements (including the coupling capacitors) of the device are implemented using interdigitated capacitors, whereas the inductive elements are realized using long narrow superconducting lines. Unlike the microstrip resonator JPC, the compact

resonator JPC does not have higher harmonic resonances. The next closest resonance of this structure resides above $4\omega_a$, therefore the pump applied at $\omega_a + \omega_b$ can be considered stiff to a very good approximation. Other advantages of this realization are: (1) small size, with dimensions much smaller than the wavelengths corresponding to the resonance frequencies, (2) no requirement of a definite ground plane, unlike the MRJ, (3) greater flexibility in engineering the characteristic impedance of the resonators higher or lower than 50Ω , (4) higher internal quality factor resonators than the microstrip design. On the other hand, the main disadvantages of this design are: (1) the narrow lines and the interdigitated capacitors (as well as the lines connecting them) have parasitic capacitances and parasitic inductances associated with them, therefore scaling these devices to match a certain frequency or certain characteristic impedance requires using a microwave simulation tool, (2) there is a limit to how big the capacitance can be using the interdigitated configuration (values above 0.5 pF is difficult to achieve), therefore engineering characteristic impedances below 30Ω is not quite feasible with this design.

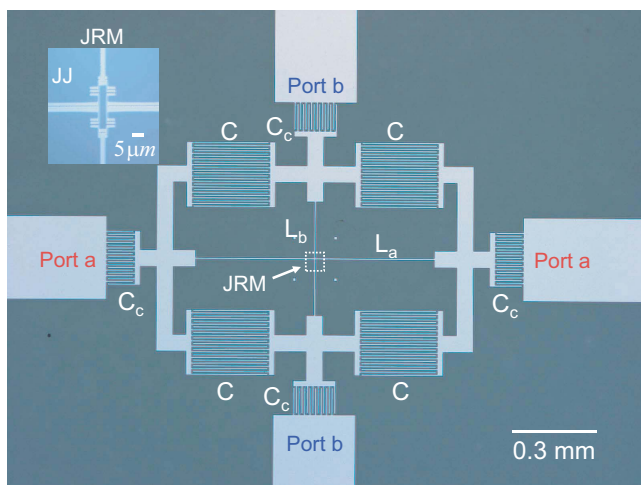


FIG. 10: (Color online). Optical microscope image of a compact resonator JPC (CRJ). The device consists of four equal interdigitated capacitors denoted C and two inductive elements denoted L_a and L_b which are realized using narrow superconducting lines of different lengths. The JRM of the device resides at the intersection of the two lines. An optical image of the JRM is shown in the inset. The CRJ is coupled to 50Ω microstrip feedlines via interdigitated capacitors denoted C_c .

C. Shunted JPC (SJ)

In this subsection we discuss a third promising design called the capacitively and inductively shunted JPC (SJ) which is still a work in progress in our lab. In this version

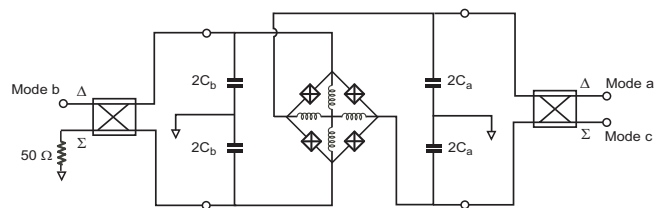


FIG. 11: Circuit model of the Shunted JPC (SJ).

of the JPC, the capacitive elements are parallel plate capacitors and the inductive elements are mainly Josephson junctions. A schematic circuit model of the SJ is drawn in Fig. 11. It is straightforward to show that the SJ model has two differential eigenmodes with angular resonance frequencies $\omega_a = 1/\sqrt{L'_J C_a}$, $\omega_b = 1/\sqrt{L'_J C_b}$, where L'_J corresponds to the equivalent inductance of the JRM shunted by linear inductors³¹, as shown in Fig. 11. The main purpose of these shunting inductors is to eliminate the hysteretic flux response of the JRM and extend the frequency tunability of the device beyond the bandwidth limit of the resonators. Such frequency tunability is achieved by varying the flux threading the loop which, in turn, varies L'_J . Note that the addition of these shunting inductors can be employed in other realizations of the JPC also, such as the MRJ, as shown in Ref.³¹ and the CRJ. It is important to emphasize, however, that the main difference between the SJ and the CRJ or MRJ schemes is that the shunted JRM in the SJ design is the only inductive element in the circuit that forms an integral part of the resonators a and b . Thus, the larger lumped capacitors employed in the SJ design play a crucial role in keeping the resonance frequencies of the device below 10 GHz.

Similar to the Josephson bifurcation amplifier (JBA) implementation¹⁵, the plate capacitors in the SJ design can be made of Nb electrodes separated by a thin SiN dielectric layer. Using plate capacitors in this realization has two advantages: (1) the plate capacitors can be made very large, i.e. their capacitance can vary in the range $1 - 40 \text{ pF}$, (2) they are easy to design as their capacitance scales linearly with the electrode area. Furthermore, due to the lumped nature of the capacitive and inductive elements in the SJ design and the fact that the capacitors can be large, the SJ has three important advantages over the previous designs: (1) the characteristic impedance of the resonators can be of the order of a few ohms, which yields an improved coupling between the resonators and the JRM, (2) due to the impedance mismatch between the characteristic impedance of the resonators and the 50Ω feedlines, the coupling capacitors are unnecessary to achieve low external Q and the feedlines can be connected directly to the resonators, (3) the maximum input power of the amplifier can be increased by increasing the critical current of the JRM junctions while keeping the

resonance frequencies fixed by enlarging the capacitors.

V. EXPERIMENTAL RESULTS

The set of JPC parameters which can be directly measured in an experiment are: the angular resonance frequencies of the resonators a and b ω_a, ω_b , the inverse of residence times of photons at resonance γ_a, γ_b , the participation ratios p_a, p_b , the maximum input power which the device can handle with no applied pump tone P_a^{\max}, P_b^{\max} , and the maximum measured gain at vanishing input power G_0^{\max} .

One way to find p_a, p_b is by measuring ω_a, ω_b as a function of applied magnetic flux threading the JRM loop. To establish this relation, we model the resonators near resonance as an LC oscillator with effective inductance $L_{a,b}$ and effective capacitance $C_{a,b}$. In this model, the bare angular resonance frequencies of the device (with the junctions) ω_a, ω_b , can be written as

$$\omega_{a,b}(\varphi) = \frac{1}{\sqrt{C_{a,b}(L_{a,b} + L_J(\varphi))}}, \quad (105)$$

where $L_J(\varphi)$ is the effective Josephson inductance of the JRM given by

$$L_J(\varphi) = \frac{L_J}{\cos\left(\frac{\varphi}{4}\right)} \quad (106)$$

with $\varphi = 2\pi\Phi/\Phi_0$. By calculating the derivative of $\omega_{a,b}(\varphi)$ with respect to the reduced flux φ , one gets

$$\frac{1}{\omega_{a,b}} \frac{d\omega_{a,b}}{d\varphi} = -\frac{1}{8} \tan\left(\frac{\varphi}{4}\right) \frac{L_J(\varphi)}{(L_{a,b} + L_J(\varphi))}, \quad (107)$$

$$= -\frac{1}{8} \tan\left(\frac{\varphi}{4}\right) p_{a,b}(\varphi). \quad (108)$$

Hence, at the device working point $\Phi = \Phi_0/2$ ($\varphi = \pi$), $p_{a,b}$ reads

$$p_{a,b} = -8 \left(\frac{1}{\omega_{a,b}} \frac{d\omega_{a,b}}{d\varphi} \right) \Big|_{\varphi=\pi}. \quad (109)$$

Furthermore, using Eq. (81) and the measured values P_a^{\max}, P_b^{\max} , one can infer the Josephson energy $E_J^{a,b}$ which is available for amplification

$$E_J^{a,b} = p_{a,b} \frac{P_{a,b}^{\max}}{\gamma_{a,b}}. \quad (110)$$

It is important to mention that, in our experiments, we find that this value is lower by about one order of magnitude than the Josephson energy of the junctions at

the working point $E_J = I_0\varphi_0/\sqrt{2}$, where I_0 is evaluated using dc resistance measurement of the junctions.

Using Eqs. (50) and (54) for the case of maximum gain G_0^{\max} yields

$$g_3^2 \bar{n}_{c,\rho \rightarrow 1} = \frac{\gamma_a \gamma_b}{4} \frac{\sqrt{G_0^{\max}} - 1}{\sqrt{G_0^{\max}} + 1}, \quad (111)$$

which in the limit of high gains gives an upper bound on the product $g_3^2 \bar{n}_{c,\rho \rightarrow 1}$

$$g_3^2 \bar{n}_{c,\rho \rightarrow 1} \leq \frac{\gamma_a \gamma_b}{4}. \quad (112)$$

Here $\bar{n}_{c,\rho \rightarrow 1}$ is the number of pump photons in the device at G_0^{\max} . In Figs. (12), (13), (14) we plot on logarithmic

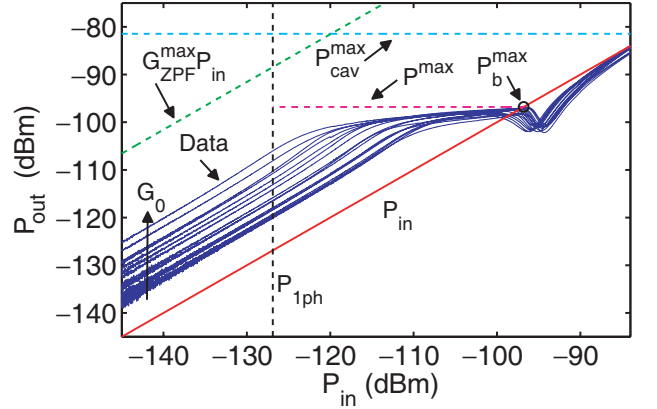


FIG. 12: (Color online). Output power P_{out} measurement of a CRJ amplifier (device A) as a function of input power P_{in} measured at ω_b . The data curves plotted in blue correspond to different G_0 setpoints obtained for different pump powers. The red line corresponds to 0 dB (unity gain) where $P_{\text{out}} = P_{\text{in}}$. The dashed black vertical line indicates the input power of 1 photon at the signal frequency per inverse dynamical bandwidth of the device at $G_0 = 20$ dB. The top horizontal line labelled P_{cav}^{\max} corresponds to the maximum circulating power in the resonator cavity given by Eq. (82). The green line corresponds to an upper limit on the device gain set by the saturation of the amplifier due to zero-point fluctuations given by Eq. (87). The dashed magenta line is a theoretical prediction for P_{out}^{\max} , which corresponds to the maximum circulating power in the device given by Eq. (114). The measured and calculated parameters of this device (A) are listed in table III.

scale the output power P_{out} of three different JPCs with different characteristics as a function of input power P_{in} . For simplicity, we refer to the three devices as A, B and C respectively. The parameters of the three devices are listed in table III. The data curves plotted in blue are measured at resonance and satisfy the relation

$$P_{\text{out}} = G(P_{\text{in}}, G_0) P_{\text{in}}, \quad (113)$$

where $G(P_{\text{in}}, G_0)$ is the amplifier gain. This depends on P_{in} and G_0 , the device gain for $P_{\text{in}} = 0$ which is set by the applied pump power. In this measurement, we apply a fixed pump power and vary P_{in} treating G_0 as a parameter. In log units, the device gain translates into a vertical offset from the 0 dB baseline (red line) which corresponds to $P_{\text{out}} = P_{\text{in}}$.

As expected, the devices maintain an almost constant gain G_0 as a function of P_{in} before they saturate and their gain drops for elevated input powers. However, as can be seen in Figs. (12), (13), (14), the three devices exhibit qualitatively different behaviors in the vicinity of their maximum input power, which correspond to different saturation mechanisms taking place in the device as will be discussed shortly. Note that the order in which the different results are presented in this section does not depend on the specific implementation of the device (see Sec. IV) but rather on the saturation mechanism involved in each case.

In Fig. 12, device A exhibits almost a plateau in P_{out} as it reaches its maximum input power for different G_0 setpoints. This result can be explained by assuming a stiff pump for which Eq. (83) applies. By employing P_b^{max} , measured with no applied pump tone, we plot the dashed magenta line labelled P^{max} which corresponds to

$$P_{\text{out}}^{\text{max}} = P_b^{\text{max}}. \quad (114)$$

The dashed black vertical line indicates the input power of 1 photon at the signal frequency per inverse dynamical bandwidth of the device at $G_0 = 20$ dB. In practice, as we discuss in Sec. VI, the usable region in the parameter space of the device with respect to gain, bandwidth and maximum input power lies within the boundaries of the fictitious triangle formed by the magenta, red and black lines. Furthermore, in Figs. (12), (13), (14) we plot two fundamental limits on the maximum gain $G_{\text{ZPF}}^{\text{max}}$ (green line) which corresponds to saturation of the device due to amplified zero-point fluctuations and the maximum circulating power $P_{\text{cav}}^{\text{max}}$ (cyan line), given by Eq. (87) and Eq. (82) respectively.

The fact that these lines lie considerably above the experimental data in Figs. (12), (13), (14), suggests that the energy threshold, at which nonlinear effects in these devices become significant, is much lower than the Josephson energy of the junctions, i.e. $E_J^{a,b} \ll E_J$.

In contrast to Fig. 12, the data curves shown in Fig. 13 for device B, exhibit a gradual decrease in the gain in the vicinity of the maximum input power which can be explained in terms of pump depletion effect discussed in Sec. III. The maximum bound P^{max} indicated by the solid magenta line corresponds to $P_{\text{out}}^{\text{max}} = G_0 P_{\text{in}}^{\text{max}}$, where in this case $P_{\text{in}}^{\text{max}}$ satisfies the inequality 103 and is given by

$$P_{\text{in}}^{\text{max}} = \frac{P_a^{\text{max}}}{G_0^{3/2}}. \quad (115)$$

On the other hand the data curves shown in Fig. 14 for

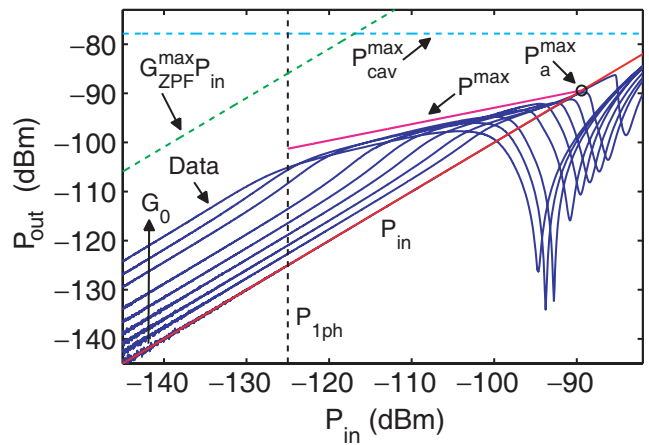


FIG. 13: (Color online). Output power P_{out} measurement of a MRJ amplifier (device B) as a function of input power P_{in} measured at ω_a . The data curves plotted in blue correspond to different G_0 setpoints obtained for different pump powers. The red line corresponds to 0 dB (unity gain) where $P_{\text{out}} = P_{\text{in}}$. The dashed black vertical line indicates the input power of 1 photon at the signal frequency per inverse dynamical bandwidth of the device at $G_0 = 20$ dB. The top horizontal line labelled $P_{\text{cav}}^{\text{max}}$ corresponds to the maximum circulating power in the resonator cavity given by Eq. (82). The green line corresponds to an upper limit on the device gain set by the saturation of the amplifier due to zero-point fluctuations given by Eq. (87). The solid magenta line is a theoretical prediction for $P_{\text{in}}^{\text{max}}$ of the device and the corresponding $P_{\text{out}}^{\text{max}}$ due to pump depletion effect given by Eq. (115). The measured and calculated parameters of this device (B) are listed in table III.

device C exhibit an abrupt drop in the device gain in the vicinity of $P_{\text{in}}^{\text{max}}$ of the device, which indicates that the device enters an unstable regime at elevated input powers. As can be seen in this case the solid magenta line — which satisfies $P_{\text{out}}^{\text{max}} = G_0 P_{\text{in}}^{\text{max}}$, where $P_{\text{in}}^{\text{max}}$ is given by Eq. (115) — lies above the experimental data. This suggests that the maximum input power in this sample, which displays a steeper power scaling than Eq. (115), is mainly limited by nonlinear effects arising from higher order terms in the Hamiltonian of the system and cannot be attributed to a pump depletion effect alone. It is worthwhile noting that a similar power scaling for the maximum input power has been observed as well for an MRJ amplifier in Ref. 12.

To understand which properties are responsible for the different gain behaviors exhibited by devices A, B and C, we point out a few important distinctions in their design (respective parameters are listed in table III). The data in Fig. 12 (device A) and Fig. 14 (device C) is measured on JPC devices realized using the CRJ configuration which yields, in general, a stiff pump response as explained in Sec. IV (B). However, the main two differences between devices A and C are: (1) device A has a narrower bandwidth as compared to C (70 MHz vs. 142 MHz) and (2) the JRM junctions in A have a smaller I_0 compared to

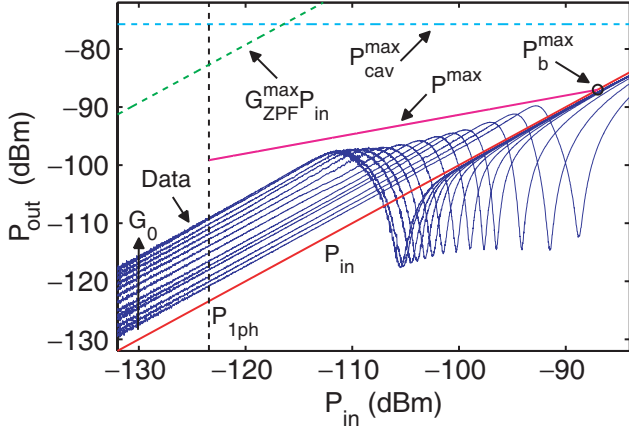


FIG. 14: (Color online). Output power P_{out} measurement of another CRJ amplifier (device C, with different parameters from device A) as a function of input power P_{in} measured at ω_b . The data curves plotted in blue corresponds to different G_0 setpoints obtained for different pump powers. The data curves of this device exhibit abrupt drop in the gain in the vicinity of the maximum input powers which suggests that the device enters an unstable regime at elevated input powers. The red line corresponds to 0 dB (unity gain) where $P_{\text{out}} = P_{\text{in}}$. The dashed black vertical line indicates the input power of 1 photon at the signal frequency per inverse dynamical bandwidth of the device at $G_0 = 20$ dB. The top horizontal line labelled $P_{\text{cav}}^{\text{max}}$ corresponds to the maximum circulating power in the resonator cavity given by Eq. (82). The green line correspond to an upper limit on the device gain set by the saturation of the amplifier due to zero-point fluctuations given by Eq. (87). The solid magenta line is a theoretical prediction for $P_{\text{in}}^{\text{max}}$ of the device and the corresponding $P_{\text{out}}^{\text{max}}$ due to pump depletion effect given by Eq. (115). The measured and calculated parameters of this device (C) are listed in table III.

those in C ($2 \mu\text{A}$ vs. $4 \mu\text{A}$). The relatively large bandwidth of device C leads to a larger dynamical bandwidth 14 MHz at $G_0 = 16$ dB, as opposed to 10 MHz achieved in device A for the same gain, and also yields (with the larger I_0 of device C) higher $P_{a,b}^{\text{max}}$ values. However, the large bandwidth translates into a lower pQ product for C as compared to A, thus making it more susceptible to parametric oscillation (at high gains or high input powers) as implied by inequality (85).

Device B, on the other hand, exhibits a pump depletion effect as shown in Fig. 13. This can be attributed to its MRJ configuration, which, in general, exhibits a less stiff pump response than the CRJ, due to the presence of high order modes as explained in Sec. IV (A). Furthermore, as opposed to the MRJ amplifier in Ref. 12 with an idler frequency of 6.4 GHz, device B has a higher idler frequency of 15 GHz which leads to a higher pQ product.

Parameter \ Device	A	B	C
Design	CRJ	MRJ	CRJ
$\omega_a/2\pi$ (GHz)	6.576	8.436	7.051
$\omega_b/2\pi$ (GHz)	6.873	15.087	7.673
$\omega_3/2\pi$ (GHz)	13.449	23.523	14.724
$\gamma_a/2\pi$ (MHz)	69	116	79
$\gamma_b/2\pi$ (MHz)	71	250 ± 25	142
Q_a, Q_b	94, 96	73, 60	89, 54
p_a, p_b	0.02	0.03, 0.05	0.03
$p_a p_b Q_a Q_b$	8.1	6.6	4.3
I_0 (μA)	2	3	4
$P_{\text{cav}}^{\text{max}}$ (dBm)	-82	-77	-76
$P_{a,b}^{\text{max}}$ (dBm)	-97	-89	-87
$P_{1\text{ph}}$ (dBm)	-127	-125	-123
$G_{\text{ZPF}}^{\text{max}}$ (dB)	38	39	40
G_0^{max} (dB)	22	20	16
$g_3 \bar{n}_{c,\rho \rightarrow 1}^{1/2}/2\pi$ (MHz)	33	77	45

TABLE III: Parameters of JPCs A, B and C. Precision is last significant digit unless indicated otherwise.

VI. REQUIREMENTS FOR QUBIT READOUT

One of the leading architectures which is used to manipulate and readout the state of superconducting qubits such as transmons and fluxoniums^{32,33} is circuit Quantum Electrodynamics (cQED). In such a system a quantum non-demolition measurement of the qubit state can be performed using dispersive readout in which the frequencies of the qubit and the cavity are detuned. As a result, the qubit and the cavity interact via exchanging virtual microwave photons³⁴ and the qubit state gets encoded in the output microwave field of the cavity. However, since the energy of microwave photons is very small, the detection of single photons is difficult especially considering the fact that state-of-the-art cryogenic amplifiers (i.e. high electron mobility transistor (HEMT)³⁵) following the cQED setup add noise to the input signal, equivalent to about 20 – 40 photons at the signal frequency. Therefore, adding a quantum-limited amplifier in series between the cQED sample and the HEMT amplifier can substantially decrease the noise temperature of the system and enable real-time tracking of the qubit state^{9,10}. The desired requirements of a Josephson parametric amplifier for such high-fidelity qubit readout can be summarized as follows:

- A center frequency in the range 5 – 12 GHz which is widely used in readout cavities of superconducting qubits.
- A large power gain on the order of 20 dB in order to beat the noise of the following amplifier, i.e. the HEMT.
- A minimum added noise to the signal, equivalent to

assumed an available Josephson energy 10 times smaller than $E_J/\sqrt{2}$ of the junctions, in agreement with experimental conditions. Finally, we verify that the set of parameters of the optimized device satisfy the inequalities $\bar{n}_c^{\max} = 3.7 \cdot 10^3 > \bar{n}_c^{\text{po}} = 1.3 \cdot 10^3 > \bar{n}_c^{20\text{dB}} = 10^3$.

VII. CONCLUSION

We have addressed in this paper a new type of quantum signal processing device based on Josephson tunnel junctions. In contrast with the devices based on SQUIDS and driven non-linear Josephson oscillators, it performs a fully non-degenerate three-wave mixing in which the modes of the signal, pump and idler are separate both spatially and temporally. The heart of the device consists of a ring modulator constructed from four Josephson junctions arranged in a loop. Both quantum-limited amplification and noiseless frequency conversion are possible with this device, and the characteristics of these analog signal processing operations are entirely calculable analytically. We have established the limitations preventing the simultaneous maximization of photon number gain, bandwidth and dynamic range. Nevertheless, we have shown that a device satisfying all the requirements of superconducting qubit readout is realizable with present day technology.

Acknowledgments

Discussions with Flavius Schackert, Michael Hatridge, Nicolas Bergeal, Benjamin Huard and Ananda Roy are gratefully acknowledged. The assistance of Michael Power and Luigi Frunzio in the fabrication process is highly appreciated. This work was supported by Yale University, NSF, IARPA, ARO and College de France.

Appendix: Quantum signals propagating along a transmission line and input-output formalism

This appendix treats quantum-mechanically the damping of a circuit by a resistance modelled as a semi-infinite transmission line, as shown in Fig. 16. It borrows heavily from the book by Gardiner and Zoller³⁶ but uses slightly different notations that are adapted to the specificities of our Josephson circuits. We first describe an infinite transmission line extending from $x = -\infty$ to $x = +\infty$. Later, we will cut the line at $x = 0$ and replace the left portion by two terminals of the circuit.

Infinite transmission line

The capacitance and inductance per unit length of the line are C_ℓ and L_ℓ , respectively. The equations obeyed

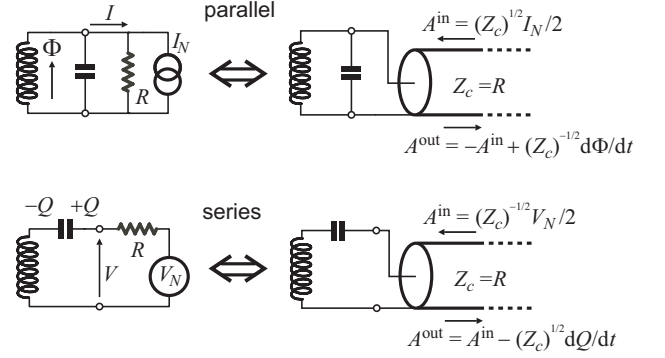


FIG. 16: The damping of a circuit by a resistance R can take place in a parallel or series way, depending on whether the resistance is placed across a branch or in series with it. The Nyquist model represents the resistance by a transmission line with characteristic impedance $Z_c = R$. The noise source associated with the resistance (fluctuation-dissipation theorem) is a parallel current source in the parallel case and a series voltage source in the series case. The noise source is replaced in the Nyquist model by incoming thermal radiation whose amplitude A^{in} is the square root of the power flux of the radiation (A^{in} should not be associated to a vector potential and is rather like the square root of the length of the Poynting vector).

by the current I along and the voltage V across the line are

$$-\frac{\partial}{\partial x} V(x, t) = L_\ell \frac{\partial}{\partial t} I(x, t), \quad (116)$$

$$-\frac{\partial}{\partial x} I(x, t) = C_\ell \frac{\partial}{\partial t} V(x, t), \quad (117)$$

in which, for the moment, we treat the fields classically. The characteristic impedance and propagation velocity are given by

$$Z_c = \sqrt{\frac{L_\ell}{C_\ell}}, \quad (118)$$

$$v_p = \sqrt{\frac{1}{L_\ell C_\ell}}. \quad (119)$$

In order to solve Eqs. (116) and (117), we introduce two new fields: the left-moving and right-moving wave amplitudes,

$$A^\rightarrow(x, t) = \frac{1}{2} \left[\frac{1}{\sqrt{Z_c}} V(x, t) + \sqrt{Z_c} I(x, t) \right], \quad (120)$$

$$A^\leftarrow(x, t) = \frac{1}{2} \left[\frac{1}{\sqrt{Z_c}} V(x, t) - \sqrt{Z_c} I(x, t) \right], \quad (121)$$

which have the advantage of treating currents and voltage on the same footing (note that these amplitudes are not directly related to the vector potential). The dimension of these fields is $[\text{watt}]^{1/2}$ and they are normalized

such that the total power P traversing, in the forward direction, a section of the line at position x and time t is given by

$$P(x, t) = [A^\rightarrow(x, t)]^2 - [A^\leftarrow(x, t)]^2. \quad (122)$$

The quantity P here plays the role of the Poynting vector in full 3D electrodynamics. Each of the terms at the right hand side of the last equation is thus the separate contribution of the corresponding wave to the total power flow.

When solving Eqs. (116-117), we find

$$\frac{\partial}{\partial x} A^\rightleftharpoons(x, t) = \mp \frac{1}{v_p} \frac{\partial}{\partial t} A^\rightleftharpoons(x, t). \quad (123)$$

This relation means that A^\rightleftharpoons does not depend separately on x or t but a combination of both and thus:

$$\begin{aligned} A^\rightarrow(x, t) &= A^\rightarrow\left(x = 0, t - \frac{x}{v_p}\right) = A^\rightarrow(x - v_p t, t = 0), \\ A^\leftarrow(x, t) &= A^\leftarrow\left(x = 0, t + \frac{x}{v_p}\right) = A^\leftarrow(x + v_p t, t = 0). \end{aligned} \quad (124)$$

The properties of the wave amplitude can be summarized by writing

$$A^\rightleftharpoons(x, t) = A_0^\rightleftharpoons(\tau), \quad (125)$$

$$\tau = t + \frac{\varepsilon^\rightleftharpoons}{v_p} x, \quad (126)$$

$$\varepsilon^\rightleftharpoons = \mp 1. \quad (127)$$

Note that the detailed definition of the retardation τ depends on the wave direction. We now turn to the energy density $U(x, t)$, related to P by the local energy conservation law

$$\frac{\partial U}{\partial t} = -\frac{\partial P}{\partial x}. \quad (128)$$

Combining Eqs. (122) and (123), we get

$$\begin{aligned} &\frac{\partial U(x, t)}{\partial t} \\ &= \frac{2}{v_p} \left[A^\rightarrow(x, t) \frac{\partial}{\partial t} A^\rightarrow(x, t) + A^\leftarrow(x, t) \frac{\partial}{\partial t} A^\leftarrow(x, t) \right], \\ &= \frac{1}{v_p} \frac{\partial}{\partial t} \left\{ [A^\rightarrow(x, t)]^2 + [A^\leftarrow(x, t)]^2 \right\}. \end{aligned} \quad (129)$$

The total energy of the line at time t is, thus³⁷,

$$H = \frac{1}{v_p} \int_{-\infty}^{+\infty} \left\{ [A^\rightarrow(x, t)]^2 + [A^\leftarrow(x, t)]^2 \right\} dx. \quad (130)$$

When H in Eq. (130) is considered as a functional of dynamical field variables A^\rightarrow and A^\leftarrow , the equation of

motion Eq. (123) can be recovered from Hamilton's equation of motion as

$$\frac{\partial}{\partial t} A^\rightleftharpoons(x, t) = -\{H, A^\rightleftharpoons(x, t)\}_{P.B.}, \quad (131)$$

on imposing the Poisson bracket

$$\{A^\rightleftharpoons(x_1, t_1), A^\rightleftharpoons(x_2, t_2)\}_{P.B.} = \frac{1}{2} \frac{\partial}{\partial(\tau_1 - \tau_2)} \delta(\tau_1 - \tau_2). \quad (132)$$

Therefore, from the classical-quantum correspondence involving the replacement of Poisson brackets by commutators, we find that the quantum operator version $\hat{A}^\rightleftharpoons$ of the fields satisfy the commutation relation

$$\left[\hat{A}^\rightleftharpoons(x_1, t_1), \hat{A}^\rightleftharpoons(x_2, t_2) \right] = \frac{i\hbar}{2} \frac{\partial}{\partial(\tau_1 - \tau_2)} \delta(\tau_1 - \tau_2), \quad (133)$$

which is analogous to the commutation relation between the electric and magnetic field in 3-D quantum electrodynamics. Note that the fields are Hermitian at this stage. Introducing the Fourier transform,

$$\hat{A}^\rightleftharpoons[\omega] = \frac{1}{\sqrt{2\pi}} \int_{-\infty}^{+\infty} \hat{A}^\rightleftharpoons(x = 0, \tau) e^{i\omega\tau} d\tau, \quad (134)$$

where the Fourier components (which are now non-hermitian operators) satisfy

$$\hat{A}^\rightleftharpoons[\omega]^\dagger = A^\rightleftharpoons[-\omega], \quad (135)$$

we can also write the Hamiltonian as

$$\sum_{\sigma=\rightleftharpoons} \int_{-\infty}^{+\infty} \hat{A}^\sigma[\omega] \hat{A}^\sigma[-\omega] d\omega. \quad (136)$$

The field operators in the frequency domain satisfy

$$\left[\hat{A}^\rightleftharpoons[\omega_1], \hat{A}^\rightleftharpoons[\omega_2] \right] = \frac{\hbar}{4} (\omega_1 - \omega_2) \delta(\omega_1 + \omega_2). \quad (137)$$

We now introduce the usual quantum field annihilation operators

$$a^\rightarrow[\omega] = \frac{\hat{A}^\rightarrow[\omega]}{\sqrt{\hbar|\omega|/2}} = a^\rightarrow[-\omega]^\dagger, \quad (138)$$

$$a^\leftarrow[\omega] = \frac{\hat{A}^\leftarrow[\omega]}{\sqrt{\hbar|\omega|/2}} = a^\leftarrow[-\omega]^\dagger. \quad (139)$$

They satisfy the commutation relations

$$[a^\rightleftharpoons[\omega_1], a^\rightleftharpoons[\omega_2]] = \text{sgn}\left(\frac{\omega_1 - \omega_2}{2}\right) \delta(\omega_1 + \omega_2). \quad (140)$$

It is useful to note that since

$$a^\rightleftharpoons[\omega] = a^\rightleftharpoons[-\omega]^\dagger, \quad (141)$$

Eq. (140) exhaustively describes all possible commutator cases.

In the thermal state of the line, at arbitrary temperature (including $T = 0$),

$$\langle a^{\rightleftharpoons}[\omega_1] a^{\rightleftharpoons}[\omega_2] \rangle = S_{a^{\rightleftharpoons}a^{\rightleftharpoons}} \left[\frac{\omega_1 - \omega_2}{2} \right] \delta(\omega_1 + \omega_2), \quad (142)$$

where

$$S_{a^{\rightleftharpoons}a^{\rightleftharpoons}}[\omega] = \text{sgn}(\omega) N_T(\omega). \quad (143)$$

When ω is strictly positive $N_T(\omega)$ is the number of available photons per unit bandwidth per unit time travelling on the line in a given direction around frequency ω

$$N_T(\omega) = \frac{1}{\exp\left(\frac{\hbar\omega}{k_B T}\right) - 1} \quad (144)$$

$$= \frac{1}{2} \left[\coth\left(\frac{\hbar\omega}{2k_B T}\right) - 1 \right]. \quad (145)$$

Negative frequencies ω correspond to the possibility of emitting photons into the line

$$N_T(-|\omega|) = -N_T(|\omega|) - 1. \quad (146)$$

The Bose-Einstein expression $N_T(\omega)$ is expected from the Hamiltonian of the line, which reads, with the a operators,

$$H = \frac{\hbar}{2} \sum_{\sigma=\rightleftharpoons} \int_{-\infty}^{+\infty} |\omega| a^{\sigma}[\omega] a^{\sigma}[-\omega] d\omega. \quad (147)$$

We can now give the expression for the anticommutator of the fields

$$\begin{aligned} \langle \{ a^{\rightleftharpoons}[\omega_1], a^{\rightleftharpoons}[\omega_2] \} \rangle_T &= 2\mathcal{N}_T \left[\frac{\omega_1 - \omega_2}{2} \right] \delta(\omega_1 + \omega_2) \\ &= \text{sgn}\left(\frac{\omega_1 - \omega_2}{2}\right) \coth\left(\frac{\hbar(\omega_1 - \omega_2)}{4k_B T}\right) \delta(\omega_1 + \omega_2). \end{aligned} \quad (148)$$

Equation (30) with no external drive is identical to Eq. (148)

$$\mathcal{N}_T[\omega] = \frac{\text{sgn}(\omega)}{2} \coth\left(\frac{\hbar\omega}{2k_B T}\right) \quad (149)$$

$$= \text{sgn}(\omega) \left[N_T(|\omega|) + \frac{1}{2} \right]. \quad (150)$$

We now introduce the forward-propagating and backward-propagating voltage and current amplitudes obeying

$$V^{\rightarrow}(x, t) = \sqrt{Z_c} A^{\rightarrow}(x, t), \quad (151)$$

$$V^{\leftarrow}(x, t) = \sqrt{Z_c} A^{\leftarrow}(x, t), \quad (152)$$

$$I^{\rightarrow}(x, t) = V^{\rightarrow}(x, t) / Z_c, \quad (153)$$

$$I^{\leftarrow}(x, t) = V^{\leftarrow}(x, t) / Z_c. \quad (154)$$

Quantum-mechanically, the voltage and current amplitudes become hermitian operators

$$V^{\rightleftharpoons}(x, t) \rightarrow \hat{V}^{\rightleftharpoons}(x, t), \quad (155)$$

$$I^{\rightleftharpoons}(x, t) \rightarrow \hat{I}^{\rightleftharpoons}(x, t). \quad (156)$$

These operators, in turn, can be expressed in terms of field annihilation operators as

$$\hat{V}^{\rightleftharpoons}(x, t) = \sqrt{\frac{\hbar Z_c}{4\pi}} \int_{-\infty}^{+\infty} d\omega \sqrt{|\omega|} \hat{a}^{\rightleftharpoons}[\omega] e^{-i\omega(t \mp x/v_p)}, \quad (157)$$

$$\hat{I}^{\rightleftharpoons}(x, t) = \sqrt{\frac{\hbar}{4\pi Z_c}} \int_{-\infty}^{+\infty} d\omega \sqrt{|\omega|} \hat{a}^{\rightleftharpoons}[\omega] e^{-i\omega(t \mp x/v_p)}. \quad (158)$$

All physical operators can be deduced from these primary expressions. For instance, the transmission line charge operator, describing the charge in the line brought from one end to the position x , is

$$\hat{Q}^{\rightleftharpoons}(x, t) = i \sqrt{\frac{\hbar}{4\pi Z_c}} \int_{-\infty}^{+\infty} \frac{d\omega \sqrt{|\omega|}}{\omega} \hat{a}^{\rightleftharpoons}[\omega] e^{-i\omega(t \mp x/v_p)}. \quad (159)$$

Nyquist model of resistance: semi-infinite transmission line

We now are in a position to deal with the semi-infinite line extending from $x = 0$ to $x = \infty$, whose terminals at $x = 0$ models a resistance $R = Z_c$ [see Fig. 16]. In that half-line, the left- and right-moving propagating waves are no longer independent. We will now refer to the wave amplitude $A^{\leftarrow}(x = 0, t)$ as $A^{\text{in}}(t)$ and $A^{\rightarrow}(x = 0, t)$ as $A^{\text{out}}(t)$. The quantum-mechanical voltage across the terminal of the resistance and the current flowing into it satisfy the operator relations

$$\hat{V}(t) = \hat{V}^{\text{out}}(t) + \hat{V}^{\text{in}}(t), \quad (160)$$

$$\hat{I}(t) = \hat{I}^{\text{out}}(t) - \hat{I}^{\text{in}}(t). \quad (161)$$

These relations can be seen either as continuity equations at the interface between the damped circuit and the resistance/line, or as boundary conditions linking the semi-infinite line quantum fields $\hat{A}^{\text{in}}(t)$ and $\hat{A}^{\text{out}}(t)$. From the transmission line relations,

$$\hat{V}^{\text{out},\text{in}}(t) = R \hat{I}^{\text{out},\text{in}}(t), \quad (162)$$

we obtain

$$\hat{I}(t) = \frac{1}{R} \hat{V}(t) - 2\hat{I}^{\text{in}}(t), \quad (163)$$

$$= \frac{1}{R} \hat{V}(t) - \frac{2}{\sqrt{R}} \hat{A}^{\text{in}}(t). \quad (164)$$

For a dissipationless circuit with Hamiltonian $H_{bare}(\hat{\Phi}, \hat{Q})$, where $\hat{\Phi}$ is the generalized flux of the node electrically connected to the transmission line, and \hat{Q} its canonically conjugate operator (top panel of Fig. 16), we can write the Langevin equation,

$$\begin{aligned} \frac{d}{dt}\hat{Q} &= \frac{i}{\hbar} [H_{bare}, \hat{Q}] - \hat{I}, \\ &= \frac{i}{\hbar} [H_{bare}, \hat{Q}] - \frac{d}{Rdt}\hat{\Phi} + \frac{2}{\sqrt{R}}\hat{A}^{in}(t). \end{aligned} \quad (165)$$

The latter equation is just a particular case of the more general quantum Langevin equation giving the time evolution of any operator \hat{Y} of a system with Hamiltonian H_{bare} , which is coupled to the semi-infinite transmission line by an Hamiltonian term proportional to another system operator \hat{X} ,

$$\begin{aligned} \frac{d}{dt}\hat{Y} &= \frac{i}{\hbar} [H_{bare}, \hat{Y}] \\ &+ \frac{1}{2i\hbar} \left\{ [\hat{X}, \hat{Y}], 2R^{\zeta/2}\hat{A}^{in}(t) - R^{\zeta}\frac{d}{dt}\hat{X} \right\}. \end{aligned} \quad (166)$$

The value of ζ in Eq. (166) depends on whether the damping is ‘‘parallel’’ ($\zeta = -1$) or ‘‘series’’ type ($\zeta = +1$) [see Fig. 16]. In the parallel case, the greater the line impedance the smaller the damping, whereas in the series case the situation is reversed.

Equation (166) should be supplemented by

$$[\hat{A}^{in}(t_1), \hat{A}^{in}(t_2)] = \frac{i\hbar}{2} \frac{\partial}{\partial(t_1 - t_2)} \delta(t_1 - t_2) \quad (167)$$

and

$$\hat{A}^{out}(t) = \zeta \left[\hat{A}^{in}(t) - R^{\zeta/2} \frac{d}{dt} \hat{X} \right]. \quad (168)$$

It follows from the last three equations that the output fields have the same commutation relation as the input fields

$$[\hat{A}^{out}(t_1), \hat{A}^{out}(t_2)] = \frac{i\hbar}{2} \frac{\partial}{\partial(t_1 - t_2)} \delta(t_1 - t_2). \quad (169)$$

Quantum Langevin equation in the RWA approximation

We now consider an approximate form of the input-output formalism which is valid when the system degree of freedom consists of an oscillator with very low damping, and for which all the frequencies of interest will lie in

a narrow range around the oscillator frequency ω_a . We start from Eq. (165) and use

$$\hat{\Phi} = \Phi^{ZPF} (a + a^\dagger), \quad (170)$$

$$\hat{Q} = Q^{ZPF} \frac{(a - a^\dagger)}{i}, \quad (171)$$

where $\Phi^{ZPF} = \sqrt{\hbar Z_a/2}$ and $Q^{ZPF} = \sqrt{\hbar/2Z_a}$.

We then obtain, neglecting the effect of driving terms oscillating at twice the resonance frequency,

$$\frac{d}{dt}a = \frac{i}{\hbar} [H_{bare}, a] - \omega_a \frac{Z_a}{2R} a + \sqrt{\frac{2Z_a}{\hbar R}} \tilde{A}^{in}(t) \quad (172)$$

with

$$\tilde{A}^{in}(t) = \int_0^\infty \hat{A}^{in}[\omega] e^{-i\omega t} d\omega. \quad (173)$$

The field amplitude $\tilde{A}^{in}(t)$ is non-hermitian and contains only the negative frequency component of $A^{in}(t)$. For signals in a narrow band of frequencies around the resonance frequency, we can make the substitution

$$\sqrt{\frac{2}{\hbar\omega_a}} \tilde{A}^{in}(t) \rightarrow \tilde{a}^{in}(t), \quad (174)$$

where

$$\tilde{a}^{in}(t) = \int_0^\infty a^{in}[\omega] e^{-i\omega t} d\omega. \quad (175)$$

The input field operator $a^{in}[\omega]$ is identical to $a^{\leftarrow}[\omega]$ of the infinite line. We finally arrive at the RWA quantum Langevin equation, also referred to in the quantum optics literature as the quantum Langevin equation in the Markov approximation

$$\frac{d}{dt}a = \frac{i}{\hbar} [H_{bare}, a] - \frac{\gamma_a}{2} a + \sqrt{\gamma_a} \tilde{a}^{in}(t), \quad (176)$$

where

$$[\tilde{a}^{in}(t), \tilde{a}^{in}(t')^\dagger] = \delta(t - t'). \quad (177)$$

For any oscillator, the input output relationship is obtained from

$$\sqrt{\gamma_a} a(t) = \tilde{a}^{in}(t) - \zeta \tilde{a}^{out}(t). \quad (178)$$

It is worth noting that although a^{in} and a^{out} play the role of a^{\leftarrow} and a^{\rightarrow} in Eq. (140), only the average values of the moments of a^{in} can be imposed, a^{out} being a ‘‘slave’’ of the dynamics of a^{in} , as processed by the oscillator.

* Electronic address: baleegh.abdo@yale.edu

¹ D. I. Schuster, A. A. Houck, J. A. Schreier, A. Wallraff,

- J. M. Gambetta, A. Blais, L. Frunzio, J. Majer, B. R. Johnson, M. H. Devoret, S. M. Girvin and R. J. Schoelkopf, *Nature* **445**, 515 (2007).
- ² M. H. Devoret, S. M. Girvin and R. J. Schoelkopf, *Annalen der Physik* **16**, 767 (2007).
 - ³ M. A. Castellanos-Beltran, K. D. Irwin, G. C. Hilton, L. R. Vale, and K. W. Lehnert, *Nature Phys.* **4**, 928 (2008).
 - ⁴ N. Bergeal, F. Schackert, M. Metcalfe, R. Vijay, V. E. Manucharyan, L. Frunzio, D.E. Prober, R. J. Schoelkopf, S. M. Girvin and M. H. Devoret, *Nature* **465**, 64 (2010).
 - ⁵ B. Yurke, P. G. Kaminsky, R. E. Miller, E. A. Whittaker, A. D. Smith, A. H. Silver and R. W. Simon, *Phys. Rev. Lett.* **60**, 764 (1988).
 - ⁶ B. Yurke, L. R. Corruccini, P. G. Kaminsky, L. W. Rupp, A. D. Smith, A. H. Silver, R. W. Simon, and E. A. Whittaker, *Phys. Rev. A* **39**, 2519 (1989).
 - ⁷ R. Movshovich, B. Yurke, P. G. Kaminsky, A. D. Smith, A. H. Silver, R. W. Simon, and M. V. Schneider, *Phys. Rev. Lett.* **65**, 1419 (1990).
 - ⁸ J. D. Teufel, T. Donner, M. A. Castellanos-Beltran, J. M. Harlow and K. W. Lehnert, *Nature Nanotechnology* **4**, 820 (2009).
 - ⁹ R. Vijay, D. H. Slichter, and I. Siddiqi, *Phys. Rev. Lett.* **106**, 110502 (2011).
 - ¹⁰ M. Hatridge, S. Shankar, M. Mirrahimi, F. Schackert, K. Geerlings, T. Brecht, K. Sliwa, B. Abdo, L. Frunzio, S. Girvin, R. Schoelkopf, M. Devoret, submitted.
 - ¹¹ N. Bergeal, R. Vijay, V. E. Manucharyan, I. Siddiqi, R. J. Schoelkopf, S. M. Girvin and M. H. Devoret, *Nature Physics* **6**, 296 (2010).
 - ¹² B. Abdo, F. Schackert, M. Hatridge, C. Rigetti and M. H. Devoret, *Appl. Phys. Lett.* **99**, 162506 (2011).
 - ¹³ J. D. Teufel, T. Donner, Li, Dale, J. W. Harlow, M. S. Allman, K. Cicak, A. J. Sirois, J. D. Whittaker, K. W. Lehnert and R. W. Simmonds, *Nature* **475**, 359 (2011).
 - ¹⁴ T. Yamamoto, K. Inomata, M. Watanabe, K. Matsuba, T. Miyazaki, W. D. Oliver, Y. Nakamura and J. S. Tsai, *Appl. Phys. Lett.* **93**, 042510 (2008).
 - ¹⁵ R. Vijay, M. H. Devoret and I. Siddiqi, *Rev. Sci. Instrum.* **80**, 111101 (2009).
 - ¹⁶ I. Siddiqi, R. Vijay, F. Pierre, C. M. Wilson, M. Metcalfe, C. Rigetti, L. Frunzio, and M. H. Devoret, *Phys. Rev. Lett.* **93**, 207002 (2004).
 - ¹⁷ M. Hatridge, R. Vijay, D. H. Slichter, J. Clarke and I. Siddiqi, *Phys. Rev. B* **83**, 134501 (2011).
 - ¹⁸ B. Abdo, E. Segev, O. Shtempluck, and E. Buks, *Appl. Phys. Lett.* **88**, 022508 (2006).
 - ¹⁹ E. A. Tholen, A. Ergul, E. M. Doherty, F. M. Weber, F. Gregis and D. B. Haviland, *Appl. Phys. Lett.* **90**, 253509 (2007).
 - ²⁰ B. H. Eom, P. K. Day, H. G. LeDuc, J. Zmuidzinas, *Nature Physics* **8**, 623 (2012).
 - ²¹ Treatment of a linear dissipative environment by scattering formalism, usually employed in quantum optics. See appendix for details.
 - ²² D. M. Pozar, *Microwave Engineering*, (Wiley, 2005), Third edition.
 - ²³ E. Flurin, N. Roch, F. Mallet, M. H. Devoret, B. Huard, arXiv:1204.0732v1.
 - ²⁴ B. Abdo, K. Sliwa, F. Schackert, N. Bergeal, M. Hatridge, L. Frunzio and M. H. Devoret, manuscript in preparation.
 - ²⁵ N. Bergeal, F. Schackert, L. Frunzio and M. H. Devoret, *Phys. Rev. Lett.* **108**, 123902 (2012).
 - ²⁶ C. M. Caves, *Phys. Rev. D* **26**, 1817 (1982).
 - ²⁷ B. Huard, N. Bergeal and M. H. Devoret, *Proceedings of the International School of Physics Enrico Fermi CLXXI* 151 (2009).
 - ²⁸ R. E. Miller, W. H. Mallison, A. W. Kleinsasser, K. A. Delin and E. M. Macedo, *Appl. Phys. Lett.* **63**, 1423 (1993).
 - ²⁹ R. Vijay, E. M. Levenson-Falk, D. H. Slichter, and I. Siddiqi, *Appl. Phys. Lett.* **96**, 223112 (2010).
 - ³⁰ J. M. Manley and R. H. Rowe, *Proceedings of the IRE* 904 (1956).
 - ³¹ N. Roch, E. Flurin, F. Nguyen, P. Morfin, P. Campagne-Ibarcq, M. H. Devoret, B. Huard, *Phys. Rev. Lett.* **108**, 147701 (2012).
 - ³² J. Koch, T. M. Yu, J. Gambetta, A. Houck, D. Schuster, J. Majer, A. Blais, M. H. Devoret, S. M. Girvin and R. J. Schoelkopf, *Phys. Rev. A* **76**, 042319 (2007).
 - ³³ V. E. Manucharyan, J. Koch, L. I. Glazman and M. H. Devoret, *Science* **326**, 113 (2009).
 - ³⁴ A. Wallraff, D. I. Schuster, A. Blais, L. Frunzio, R.-S. Huang, J. Majer, S. Kumar, S. M. Girvin, R. J. Schoelkopf, *Nature* **431**, 162 (2004).
 - ³⁵ R. F. Bradley, *Nucl. Phys. B (Proc. Suppl.)* **72**, 137 (1999).
 - ³⁶ C. W. Gardiner and P. Zoller, *Quantum Noise* (Springer, 2004), Third edition.
 - ³⁷ Its value can also be obtained as the sum of the electrostatic and magnetic energy in the line

$$\frac{1}{2} \int_{-\infty}^{+\infty} \{C_\ell [V(x, t)]^2 + L_\ell [I(x, t)]^2\} dx.$$